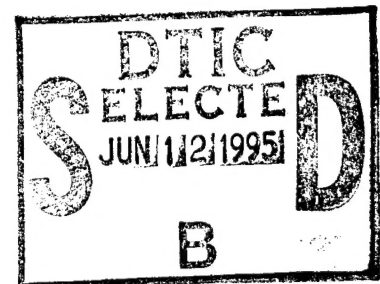


PL-TR-94-2232

DEVELOPMENT OF A GLOBAL IONOSPHERIC FORECAST MODEL

**R. W. Schunk
J. J. Sojka**

**Space Environment Corporation
399 North Main, Suite 325
Logan, UT 84321**



14 August 1994

**Final Report
5 December 1990 to 5 July 1994**

Approved for public release; distribution unlimited

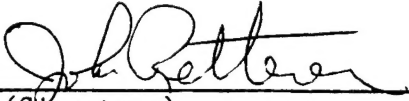


**PHILLIPS LABORATORY
Directorate of Geophysics
AIR FORCE MATERIEL COMMAND
HANSCOM AIR FORCE BASE, MA 01731-3010**

19950608 124

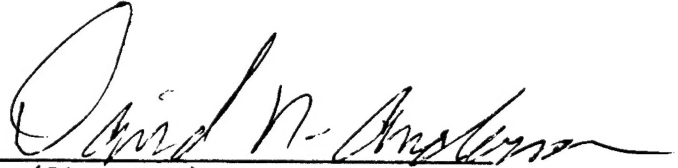
THIS QUANTITY PRINTED 6

"This technical report has been reviewed and is approved for publication:



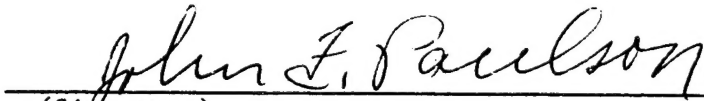
(Signature)

JOHN RETTERER
Contract Manager



(Signature)

DAVID N. ANDERSON
Branch Chief



(Signature)

JOHN F. PAULSON
Act. Division Director

This report has been reviewed by the ESC Public Affairs Office (PA) and is releasable to the National Technical Information Service (NTIS).

Qualified requestors may obtain additional copies from the Defense Technical Information Center (DTIC). All others should apply to the National Technical Information Service (NTIS).

If your address has changed, if you wish to be removed from the mailing list, or if the addressee is no longer employed by your organization, please notify PL/IM, 29 Randolph Road, Hanscom AFB, MA 01731-3010. This will assist us in maintaining a current mailing list.

Do not return copies of this report unless contractual obligations or notices on a specific document requires that it be returned.

REPORT DOCUMENTATION PAGE			Form Approved OMB No. 0704-0188	
Public reporting burden for this collection of information is estimated to average 1 hour per response, including the time for reviewing instructions, searching existing data sources, gathering and maintaining the data needed, and completing and reviewing the collection of information. Send comments regarding this burden estimate or any other aspect of this collection of information, including suggestions for reducing this burden, to Washington Headquarters Services, Directorate for Information Operations and Reports, 1215 Jefferson Davis Highway, Suite 1204, Arlington, VA 22202-4302, and to the Office of Management and Budget, Paperwork Reduction Project (0704-0188), Washington, DC 20503.				
1. AGENCY USE ONLY (Leave blank)	2. REPORT DATE 14 AUGUST 1994	3. REPORT TYPE AND DATES COVERED FINAL REPORT; 12/5/90 to 7/5/94		
4. TITLE AND SUBTITLE Development of a Global Ionospheric Forecast Model		5. FUNDING NUMBERS PE 63707F PR 4026 TA 01 WU KI		
6. AUTHOR(S) R.W. Schunk J.J. Sojka		Contract F19628-91-C-0006		
7. PERFORMING ORGANIZATION NAME(S) AND ADDRESS(ES) Space Environment Corporation 399 North Main, Suite 325 Logan, Utah 84321		8. PERFORMING ORGANIZATION REPORT NUMBER		
9. SPONSORING/MONITORING AGENCY NAME(S) AND ADDRESS(ES) Phillips Laboratory 29 Randolph Road Hanscom AFB, MA 01731-3010 Contract Manager: John Retterer/GPIM		10. SPONSORING/MONITORING AGENCY REPORT NUMBER PL-TR-94-2232		
11. SUPPLEMENTARY NOTES				
12a. DISTRIBUTION / AVAILABILITY STATEMENT Approved for public release; distribution unlimited			12b. DISTRIBUTION CODE	
13. ABSTRACT (Maximum 200 words) Our 3-dimensional, time-dependent model of the global ionosphere was streamlined in an effort to develop a computationally fast, user friendly, reliable, Ionospheric Forecast Model (IFM) for Air Weather Services. The model yields predictions for the molecular and oxygen ion densities and the ion and electron temperatures over the globe at E and F region altitudes. The model also contains a simple algorithm for predicting H ⁺ densities in the F region. The inputs needed by the IFM are global distributions of the neutral densities, temperatures, and winds, the auroral oval precipitation, the magnetospheric and dynamo electric fields, and the topside electron heat flux. Because of the model's modular construction, the IFM can readily accept different global input patterns and, hence, has the capability of being driven by real-time inputs from Air Force satellites or ground-based sites. In the current version of the model, the input patterns have been selected and the IFM is therefore self-contained and can be driven by simple geophysical indices.				
14. SUBJECT TERMS Ionospheric Model; Forecast; Ion and Electron Densities and Temperatures; Peak Densities and Heights			15. NUMBER OF PAGES 80	
			16. PRICE CODE	
17. SECURITY CLASSIFICATION OF REPORT Unclassified	18. SECURITY CLASSIFICATION OF THIS PAGE Unclassified	19. SECURITY CLASSIFICATION OF ABSTRACT Unclassified	20. LIMITATION OF ABSTRACT SAR	

Table of Contents

Executive Summary.	v
1. Introduction.	1
2. Streamlining.	2
2.1 Diffusion Equations	
2.2 Ion Chemistry	
2.3 Ion Energy Equation	
2.4 Electron Energy Equation	
2.5 Equatorial Model	
3. IFM Inputs.	7
3.1 Neutral Atmosphere	
3.2 Neutral Wind	
3.3 Magnetospheric Electric Field	
3.4 Auroral Precipitation	
3.5 Equatorial Electric Field	
3.6 Topside Heat Flow	
4. Coordinate Systems and Trajectories.	9
4.1 Coordinate Systems	
4.2 Trajectories	
5. Numerical Solution.	16
5.1 E-Region	
5.2 F-Region	
5.3 Temperatures	
5.4 H ⁺ Formulation	
5.5 Equatorial Model Implementation	
6. Validation.	30
6.1 Physics and Chemistry	
6.2 Streamlined versus Comprehensive Model	
6.3 PRIMO and VIM Studies	
7. Operating Mode.	54
References.	56
Appendix A.	58
Appendix B.	62
Appendix C.	71

EXECUTIVE SUMMARY

Our 3-dimensional, time-dependent model of the global ionosphere was streamlined in an effort to develop a computationally fast, user friendly, reliable, Ionospheric Forecast Model (IFM) for Air Weather Services. The model yields predictions for the NO^+ , O_2^+ , N_2^+ , and O^+ densities and the ion and electron temperatures over the globe at E and F region altitudes. The model also contains a simple algorithm for predicting H^+ densities in the F region. The inputs needed by the IFM are global distributions of the neutral densities, temperatures and winds, the auroral oval precipitation, the magnetospheric and dynamo electric fields, and the topside electron heat flux. Because of the model's modular construction, the IFM can readily accept different global input patterns and, hence, has the capability of being driven by real - time inputs from Air Force satellites or ground - based sites. In the current version of the model, the input patterns have been selected and the IFM is therefore self - contained and can be driven by simple geophysical indices. With a simple specification, the IFM outputs a variety of parameters, including global snapshots of N_mF_2 and h_mF_2 , density and temperature contours at fixed altitudes, altitude profiles at given locations, as well as other parameters.

Accession For	
NTIS GRA&I	<input checked="checked" type="checkbox"/>
DTIC TAB	<input type="checkbox"/>
Unannounced	<input type="checkbox"/>
Justification	
By	
Distribution/	
Availability Codes	
Dist	Avail and/or Special
A-1	

1. INTRODUCTION

Over a 20 year period, we have been actively involved in developing numerical models of the terrestrial ionosphere. The most comprehensive model that we constructed was a time - dependent, three - dimensional, multi - ion model of the global ionosphere at E and F region altitudes (cf. Schunk, 1988a; Sojka, 1989). This model yields density distributions for six ion species (NO^+ , O_2^+ , N_2^+ , O^+ , N^+ , He^+) and the electron and ion temperature distributions via a numerical solution of the coupled continuity, momentum, and energy equations. The model takes account of field-aligned diffusion, cross-field electrodynamic drifts both in the equatorial region and at high latitudes, interhemispheric flow, thermospheric winds, polar wind escape, energy-dependent chemical reactions, neutral composition changes, ion production due to solar EUV radiation, resonantly scattered radiation and auroral precipitation, electric field induced temperature anisotropies, thermal conduction, diffusion-thermal heat flow, and local heating and cooling processes. The model also takes account of the offset between the geomagnetic and geographic poles in both the northern and southern hemispheres and the bending of field lines near the magnetic equator.

With the funding from this Air Force contract, we streamlined the above global ionospheric model in order to construct a computationally efficient, user friendly, Ionospheric Forecast Model for Air Weather Services. The development effort involved four major tasks. The first task was primarily concerned with the development of the ionospheric code for a single convecting flux tube. This part of the code had to be redone so that it could be made computationally fast and efficient. This involved deriving the ambipolar diffusion equations for two ions, modifying the ion chemistry, and simplifying the ion and electron energy equations. The numerical inversion procedure also had to be redone.

The second task involved the development of the codes that describe the inputs to the ionospheric model as well as the effort involved in linking the single flux tube code to the coordinate systems and global inputs. Decisions had to be made about what coordinate systems to adopt and how many flux tubes to follow. The inputs to the ionospheric forecast model that needed to be considered were a neutral wind pattern, a neutral atmosphere, magnetospheric and equatorial electric field distributions, auroral particle precipitation patterns, the topside electron heat flux, and the mid-latitude protonospheric exchange flux. Although many of these inputs were readily available, they had to be modified so as to make them computationally efficient.

The third task involved an extensive series of validation runs. The Ionospheric Forecast Model was tested against most of the 54 diurnally reproducible runs already conducted with our full ionospheric model for the High Latitude Ionospheric Specification Model (HLISM). The IFM was also validated as part of the PRIMO and VIM programs. The last task, involved the development of graphic displays and user friendly I/O interface software.

In the following sections of this report, we provide a complete description of the current version of the IFM. We also briefly indicate the operating mode of the model, but a user manual giving detailed operating instructions will be provided separately.

2. STREAMLINING

As indicated earlier, a significant effort was devoted to streamlining our global ionospheric models, and the details are provided in the subsections that follow.

2.1. Diffusion Equations

The mathematical formulation of our 'comprehensive' ionospheric model is based on the continuity, momentum, and energy equations for four major ions (NO^+ , O_2^+ , N_2^+ , O^+) and two minor ions (He^+ , N^+). The ion diffusion equations are obtained from the momentum equations by assuming that the plasma flow is ambipolar and subsonic, which are valid assumptions at E and F region altitudes. In the original formulation, the four coupled diffusion equations are solved simultaneously over the complete altitude range from 100 to 800 km.

In the streamlined model, the E and F regions of the ionosphere are formulated separately. In the E region, we take account of the fact that diffusion is negligible and obtain the ion densities by assuming that chemical equilibrium prevails,

$$n_i = P_i / L_i \quad (1)$$

where P_i is the ion production rate, L_i the ion loss frequency, and n_i the ion density. Here, the two minor ions He^+ and N^+ are neglected, but the remaining four ions (NO^+ , O_2^+ , N_2^+ , O^+) are treated as major ions (i.e., equally important).

In the F region, the streamlining effort centered around the assumption that only NO^+ and O^+ are major ions, which has been verified over the years via numerous runs of our comprehensive ionospheric model. Therefore, the original triple - ion diffusion formulation can be replaced with the following reduced two - ion formulation:

$$\frac{\partial n_1}{\partial t} + \frac{\partial}{\partial z}(n_1 u_1) = P_1 - L_1 n_1 \quad (2)$$

$$\frac{\partial n_2}{\partial t} + \frac{\partial}{\partial z}(n_2 u_2) = P_2 - L_2 n_2 \quad (3)$$

$$u_1 = v_{1z} - D_1 \sin^2 I \left[\frac{1}{n_1} \frac{\partial n_1}{\partial z} + \frac{m_1 g}{k T_1} + \frac{1}{T_1} \frac{\partial}{\partial z}(T_1 + T_e) + \frac{(T_e / T_1)}{n_e} \frac{\partial n_e}{\partial z} \right] \quad (4)$$

$$u_2 = v_{2z} - D_2 \sin^2 I \left[\frac{1}{n_2} \frac{\partial n_2}{\partial z} + \frac{m_2 g}{k T_2} + \frac{1}{T_2} \frac{\partial}{\partial z}(T_2 + T_e) + \frac{(T_e / T_2)}{n_e} \frac{\partial n_e}{\partial z} \right] \quad (5)$$

$$n_e = n_1 + n_2 \quad (6)$$

$$n_e u_e = n_1 u_1 + n_2 u_2 \quad (7)$$

where the subscripts 1,2, and e refer to NO^+ , O^+ and electrons, respectively, and where u_i is the vertical ion drift velocity, m_i is the ion mass, T_i is the ion temperature, T_e is the electron temperature, $D_i = kT_i/(m_i\nu_i)$ is the ion diffusion coefficient, V_{iz} is the induced vertical ion drift due to neutral winds and electric fields, $\nu_i = \sum_n \nu_{in}$ is the total ion collision frequency with neutrals, k is Boltzmann's constant, g is the gravitational acceleration, z is the vertical coordinate, t is time, and I is the inclination angle of the geomagnetic field.

In the streamlined model, the minor ions N^+ and He^+ are ignored and the two remaining molecular ions (O_2^+ , N_2^+) are taken to be minor ions in chemical equilibrium. Therefore, their densities are obtained from equation (1) at all altitudes throughout the E and F regions.

In addition to the reduction of the diffusion formulation from a triple-ion to a two-ion scheme, several other simplifications were made. The small effect of temperature anisotropies was neglected, and only ion collisions with the dominant neutrals (N_2 , O) were included in the total ion collision frequency.

Note that the above diffusion formulation is valid only at middle and high latitudes, where the geomagnetic field lines are straight but inclined to the vertical. At equatorial latitudes a different formulation is employed, which will be discussed later. Also note that the separation of the E and F region formulations allows for different numerical step sizes in the two domains, which has a distinct computational advantage. This will be discussed in more detail later.

2.2. Ion Chemistry

The ion chemistry in our comprehensive ionospheric model is fairly involved. The chemical scheme includes numerous energy - dependent ion - neutral chemical reactions, electron - ion recombination, photoionization, ionization due to auroral electron precipitation and ionization resulting from resonantly scattered solar radiation. In the IFM, these processes have been simplified and/or improved.

Because some minor ions were neglected in the construction of the IFM, the ion - neutral chemical reaction scheme could be shortened. Also, over the years we found that some of the chemical reactions included in the comprehensive ionospheric model were, in fact, negligible. Therefore, the IFM could be constructed with a reduced ion - neutral chemical scheme, which is given in Table 1.

With regard to photoionization, rigorous photoproduction calculations are performed over the entire altitude range from 100 to 800 km in the comprehensive ionospheric model. Also, these calculations are performed even for large solar zenith angles ($x > 90^\circ$), which requires complex expressions for grazing incidence functions. However, experience has shown that important simplifications can be made without loss of accuracy. First, above 300 km photoionization frequencies can be introduced. The ion photoionization frequencies are calculated rigorously at 300 km and then these values are used to calculate ion production rates above this altitude. Also, ion production rates are only calculated for solar zenith angles less than 90° , which eliminates the need for the complex grazing incidence functions.

The calculation of the photoionization rates requires a knowledge of the solar spectrum and the absorption and ionization cross sections for the neutral gases in the earth's upper atmosphere. The values adopted for the IFM were obtained from Torr et al (1985), but the 37- wavelength intervals were adjusted to 11 intervals. However, checks were made to verify that the production rates obtained from the 11- interval scheme were within a few percent of those obtained from the 37 intervals. Also, in the IFM, the solar fluxes are scaled with F10.7 in order to account of solar cycle effects.

In our comprehensive ionospheric model, the ion production rates due to auroral electron precipitation are obtained by scaling the production rate profiles obtained from Knudsen et al (1977) with the auroral electron energy flux. In the IFM, our calculation of auroral production rates has been improved significantly. Our new production rate profiles are based on the auroral electron deposition code developed by Strickland et al (1976). R.E. Daniell of CPI ran this code for numerous cases and then gave us the resulting sets of production rate profiles. Specifically, he considered 27 geophysical situations, covering 3 levels of solar activity, 3 seasons, and 3 levels of geomagnetic activity. For each of the 27 geophysical situations he considered 5 auroral cases, covering different characteristic energies. For the 135 cases, production rate profiles were obtained for N_2^+ , O_2^+ and O^+ , and we incorporated these profiles in a subroutine for efficient access when plasma flux tubes convect through the auroral oval and encounter changing auroral conditions.

In the IFM, the nocturnal production rates due to resonantly scattered solar radiation are identical to those contained in our comprehensive ionospheric model. These rates are those presented by Chen and Harris (1971), which do not vary during the night.

2.3. Ion Energy Equation

The ion temperature calculation in our comprehensive ionospheric model is based on a numerical solution of a nonlinear, second order, partial differential equation. Such an equation results from the inclusion of thermal conduction and diffusion - thermal transport processes. However, these transport processes only start to have an effect at altitudes above 600-700 km and only under certain circumstances. Since an appreciable CPU savings can be obtained by neglecting these processes, they are not included in the IFM. In this case, the ion energy equation reduces to a balance between local heating (Q_i) and cooling (C_i) processes,

$$Q_i = C_i \quad (8)$$

As with our comprehensive ionospheric model, the calculation of the ion heating and cooling rates in the IFM includes thermal coupling to the electrons and neutrals as well as electric field heating. However, some simplifications were possible. Only coupling to the dominant neutrals N_2 and O was included and the small effect associated with ion temperature anisotropies was neglected.

2.4. Electron Energy Equation

Thermal conduction is a very important process for the electron gas at F - region altitudes and cannot be neglected. Therefore, in contrast to the T_i situation, a nonlinear, second order, parabolic, partial differential equation must be solved in order to obtain

electron temperatures. This equation can be expressed in the form

$$\frac{3}{2}n_e k \frac{\partial T_e}{\partial t} = \sin^2 I \frac{\partial}{\partial z} \left(K_e \frac{\partial T_e}{\partial z} \right) + Q_e - C_e \quad (9)$$

where K_e is the electron thermal conductivity, Q_e is the electron heating rate, and C_e is the electron cooling rate. In addition to thermal conduction, our comprehensive ionospheric model included electron heating via both auroral electrons and photoelectrons, thermal coupling to the ions, cooling via elastic collision with five neutral species (N_2 , O_2 , O , He , H), and cooling via several inelastic collisional processes (N_2 & O_2 rotational excitation, N_2 & O_2 vibrational excitation, and excitation of the fine structure levels of atomic oxygen).

In the IFM, only the dominant cooling processes are retained. These are elastic collisions with N_2 and O , and excitation of the fine structure levels of atomic oxygen. The neglect of the other unimportant cooling terms results in a significant CPU savings because some of these terms are long and complex. The expressions for the processes included are given in Schunk (1988a) and are not repeated here.

2.5. Equatorial Model

The mathematical formulation described above is restricted to middle and high latitudes because it is based on the assumptions that vertical gradients dominate and that the B-field lines are straight but inclined to the vertical. In this case, the plasma transport equations can be solved as a function of altitude for convecting plasma flux tubes. At equatorial latitudes, on the other hand, the geomagnetic field varies from being inclined to the vertical at higher latitudes to being horizontal at the equator. Therefore, the transport equations must be solved along the field lines taking into account both horizontal and vertical gradients. In our comprehensive model of the global ionosphere, we adopted the Sterling et al (1969) equatorial ionospheric model and modified the diffusion coefficients and ion chemistry so that they were consistent with those used in our mid-high latitude ionosphere model (cf. Sojka and Schunk, 1985).

In the IFM, we replaced the Sterling et al (1969) model with the Anderson (1973, 1981) equatorial ionospheric model. With this model, the continuity and momentum equations for O^+ and electrons are solved along a magnetic field line that extends from the northern to the southern hemisphere. The model takes into account ion-neutral chemical reactions, photoionization, diffusion, neutral winds, and electrodynamic drifts. In the most recent version, the model automatically considers a series of plasma flux tubes with different equatorial crossing altitudes so that altitude profiles can be obtained at any location. However, the series of flux tubes is at only one longitude. Typically, the equations are solved as a function of time along the series of flux tubes as they corotate and convect in response to dynamo electric fields. The lower boundary conditions are generally taken to be at 90 km in both hemispheres.

When the Anderson (1973) equatorial ionospheric model was incorporated into the IFM, several modifications were necessary. First, our E-region model is global and covers the altitude range from 90-160 km, so the lower boundary in the Anderson model was moved up to 160 km. Next, the photochemistry and diffusion coefficients were modified to

be consistent with those used in the mid - high latitude part of the IFM. Also, the model was extended from one longitude to all longitudes (global) and the input routines were modified to accept time-dependent, global inputs.

Table 1 Ion Chemistry and Reaction Rates

Reaction	Rate Coefficients, cm ³ s ⁻¹
$O^+ + N_2 \rightarrow NO^+ + O$	k_1
$O^+ + O_2 \rightarrow O_2^+ + O$	k_2
$O_2^+ + N_2 \rightarrow NO^+ + NO$	5×10^{-16}
$O_2^+ + e \rightarrow O + O$	$1.6 \times 10^{-7} (300/T_e)^{0.55}$
$N_2^+ + O \rightarrow NO^+ + N$	$1.4 \times 10^{-10} (300/T)^{0.44}; T \leq 1500^\circ K$ $5.2 \times 10^{-11} (T/300)^{0.2}; T > 1500^\circ K$
$N_2^+ + O \rightarrow O^+ + N_2$	$1 \times 10^{-11} (300/T)^{0.23}; T \leq 1500^\circ K$ $3.6 \times 10^{-12} (T/300)^{0.41}; T > 1500^\circ K$
$N_2^+ + O_2 \rightarrow O_2^+ + N_2$	$5 \times 10^{-11} (300/T)$
$N_2^+ + e \rightarrow N + N$	$1.8 \times 10^{-7} (300/T_e)^{0.39}$
$NO^+ + e \rightarrow N + O$	$4.2 \times 10^{-7} (300/T_e)^{0.85}$

3. IFM INPUTS

The IFM, like all ionospheric models, requires both magnetospheric and thermospheric inputs in order to account for ionospheric coupling to these domains. The inputs need to be time-dependent and global. At present, various empirical (i.e., statistical) models are available for almost all of the required inputs, and these input models can be 'adjusted' to accommodate real-time measurements made by Air Force satellites or at Air Force ground sites. Since it was anticipated that significant improvements in the inputs would be made in the coming years, the IFM was constructed in a modular form so that different input models could be 'plugged in' with no impact on the rest of the IFM. However, for the current version of the IFM, a specific set of input models was adopted. This first version of the IFM is therefore self-contained and driven by simple geophysical indices. The specific input models adopted are briefly described in the following subsections.

3.1. Neutral Atmosphere

The IFM requires a global distribution of the neutral densities (N_2 , O_2 , O) and temperature at altitudes between 100-800 km. These input parameters are obtained from the MSIS-90 atmospheric model (Hedin, 1991). This empirical model yields the atmospheric parameters for different solar cycle, seasonal, and geomagnetic activity levels. It also contains diurnal and longitudinal variations.

3.2. Neutral Wind

The neutral wind model adopted as an input to the IFM is the MSIS-Wind model constructed by Hedin et al (1991). This empirical model provides global distributions of the zonal and meridional wind components. As with the atmospheric model, the wind model takes account of solar cycle, seasonal, geomagnetic activity, diurnal, and longitudinal variations.

3.3. Magnetospheric Electric Field

At high latitudes, the plasma convection pattern induced by magnetospheric electric fields is crucial in determining the ionospheric densities and temperatures. Because of its importance, several empirical models of the convection electric field have been developed over the years. The models have been based on both radar data and satellite electric field data (Volland, 1978; Foster, 1983; Heelis et al, 1982; Heelis, 1984; Heppner and Maynard, 1987). For the current version of IFM, we adopted the Heppner and Maynard (1987) electric field model. This model provides magnetospheric electrostatic potential distributions over the polar regions as a function of K_p for southward IMF ($B_z < 0$) and both negative and positive B_y values.

3.4. Auroral Precipitation

Particle precipitation in the auroral oval acts as an ionization source, a source of bulk heating for the electron gas, and a thermal conduction source through our upper boundary. As with the electric field, several empirical models are available that describe the precipitating electron energy flux and characteristic energy (Feldstein and Starkov, 1967; Spiro et al, 1982; Wallis and Budzinski, 1981; Hardy et al, 1985). For the IFM, we

adopted the model by Hardy et al (1985), which is the most comprehensive model of electron precipitation developed to date. In the IFM, as the plasma flux tubes move through the auroral oval, the characteristic energy and energy flux values obtained from the Hardy et al (1985) model are used to calculate particle production rates, the bulk electron heating rate, and the thermal conduction flux through our upper boundary at the current location of the flux tube.

3.5. Equatorial Electric Field

Dynamo electric fields, generated via the thermospheric wind, are extremely important for determining equatorial electron densities. Until recently, the best empirical model of equatorial electric fields in the one developed by Richmond et al (1980), which is the one used in our comprehensive ionospheric model. Recently, however, B. Fejer and colleagues constructed a sophisticated empirical model of equatorial electric fields including longitudinal variations, and the ionospheric modelling results obtained with these electric fields have been impressive (Preble et al, 1994). Therefore, the Fejer equatorial electric field model was adopted for the IFM.

3.6. Topside Heat Flow

Escaping photoelectrons and auroral electrons lose energy to the thermal electrons at high altitudes as they traverse the ionospheric plasma. The transferred energy is then conducted down to the lower ionosphere and enters as a topside (800 km) boundary condition in the Ionospheric Forecast Model. The procedure for calculating the boundary heat flow values is identical to that used in our comprehensive ionospheric model and is not repeated here (cf. Schunk et al, 1986).

4. COORDINATE SYSTEMS AND TRAJECTORIES

The Ionospheric Forecast Model is a Lagrange - Euler hybrid model in that the continuity, momentum, and energy equations are solved on a fixed spatial grid either as a function of altitude (mid and high latitudes) or along geomagnetic field lines (low latitudes) for $\mathbf{E} \times \mathbf{B}$ convecting flux tubes of plasma (cf. Figure 1). As a consequence, coordinate systems and trajectory selection are important aspects of the IFM.

4.1. Coordinate Systems

There are two primary coordinate systems associated with the IFM, namely geographic and geomagnetic. Our comprehensive ionospheric model has always been based on a tilted offset dipole magnetic system because relatively simple transformations exist to convert from this frame to geographic. Also, we have previously assumed that the dipole magnetic coordinate system is equivalent to the magnetic invariant system. In the past, this assumption was justified because most of our studies were parametric in nature, and with latitude bins of 3 degrees and local time bins of 1 hour, the errors associated with this assumption were not significant. However, in future applications with real-time data (images, in situ satellite measurements and ground-based observations), this assumption is inappropriate. Hence, in the IFM, the more rigorous IGRF magnetic field model is adopted, and it is represented by bicubic spline interpolation tables for the magnitude, inclination, and declination. The CGMC transformation used at Phillips Laboratory/Boston is adopted for transforming between the geographic and magnetic frames.

4.2. Trajectory Selection

The magnetospheric electric field models provide contours of electrostatic potential, which coincide with the plasma streamlines at F-region altitudes (cf. Figure 1). However, decisions have to be made with regard to how many trajectories to select, how many plasma flux tubes to follow, and where the flux tubes should be placed initially. Also, account must be taken of the fact that as the plasma flux tubes convect in response to the imposed magnetospheric electric field pattern, their spatial distribution will become non-uniform because the various trajectories have different lengths and because the magnitude of the electric field varies around each trajectory differently. Therefore, a multi-step process is needed to set up and follow convecting plasma flux tubes.

In the IFM, the procedure used is shown in Figure 2. First, a latitude-longitude grid is initialized (INITGRID). Then, the Kp and other proxy indices are acquired as a time series from AWS data computers (INITACTV). These data are then used by INITTRAJ to initialize the plasma flux tubes that are to be followed. Flux tubes are placed at the center of grid cells. FLOW generates the trajectories that the plasma flux tubes are to follow. FLOW calls FLOWV1 to obtain the corotational electric field and FLOWV3 to obtain the Heppner-Maynard electric field pattern. As the flux tubes convect in response to the imposed electric fields, their spatial distribution can change markedly. Hence, every 15 minutes of model time, it is necessary to check the spatial distribution of flux tubes in the ionospheric grid to make sure there is adequate coverage everywhere. This is done in CELLCHECK. Flux tubes are deleted if too many appear in a spatial cell in order to save CPU time. Flux tube are added to a spatial cell if there is an insufficient number of flux tube in that cell. This is done in steps. FILLCELL creates a new trajectory that passes through the center of the empty cell and obtains the coordinates (CELLCOORDS). The trajectory is followed backwards in time to the previous model time interval and

interpolation is used to obtain the flux tube density profile at that previous time interval (FLOWBACK). This flux tube reverses direction and then follows the trajectory back to the present time (REVERSE). Of course, it ends up at the center of the empty cell. The routine FILLHIST creates a record of the distribution of plasma flux tubes after each IFM time interval for diagnostic purposes. Finally, before following the trajectories to the next model time interval, the model grid is advanced in MLT by the time interval (ANOTHERFLOW). This assures that corotational flux tubes stay at the midpoints of their cells and, thereby, reduces the number of flux tubes needed.

An example of how the flux tube selection procedure works is shown in Figures 3 - 5. Initially, a spatial grid with cells that are 5° in latitude and 1 hour in MLT is created for the region poleward of 40° latitude. One plasma flux tube is placed at the center of each of the 120 cells (Figure 3, bottom panel). Subsequently, the flux tubes convect in response to the corotational and magnetospheric electric fields. In this test case, a Volland (1978) symmetric two - cell convection pattern is used. As time evolves, the distribution of flux tubes becomes nonuniform. At 15-minute time intervals, the distribution is checked and cells with 10 or more flux tubes have the number reduced to 2-5, while cells with an insufficient number are augmented with new flux tubes. The resulting flux tube distribution after 1 day is shown in Figure 3 (middle panel) and after 3 days in Figure 3 (top panel). It is clear that there is always adequate coverage of the high latitude region for this $K_p = 1$ Volland convection pattern. Similar results are shown in Figures 4 and 5 for $K_p = 4$ and 7, respectively. Again, our flux tube selection procedure provides adequate coverage over the entire polar region. Note that the maximum number of flux tubes in 400 for $K_p = 7$.

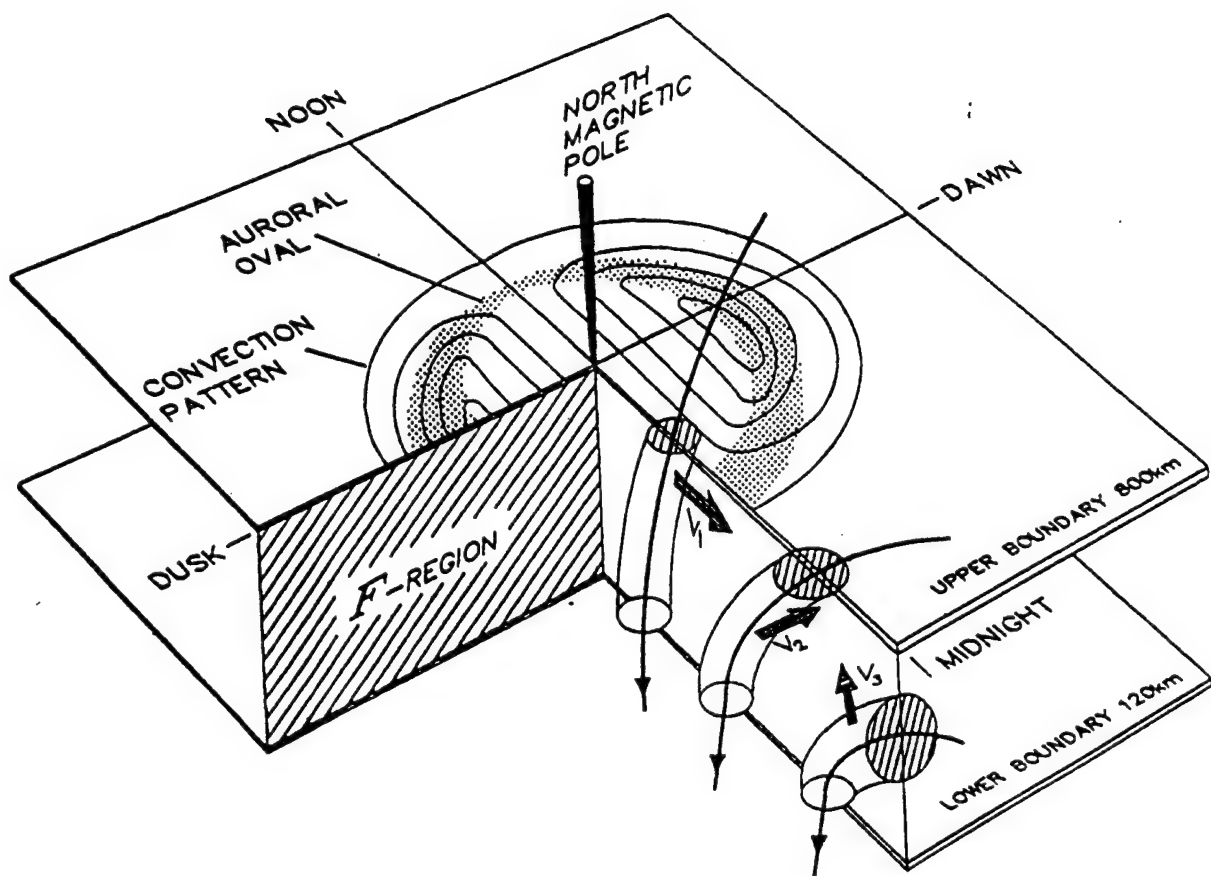


Figure 1. A schematic view of the F-region ionosphere bounded below (100km) and above (800km) extending from the north pole to the magnetic equator. The imposed magnetospheric electric fields and auroral oval are shown as contoured lines and shaded regions, respectively. A midnight cross section reveals the direction of motion of a high latitude (V_1), mid-latitude (V_2), and equatorial (V_3) plasma flux tube. From Sojka [1989].

TRAJECTORIES

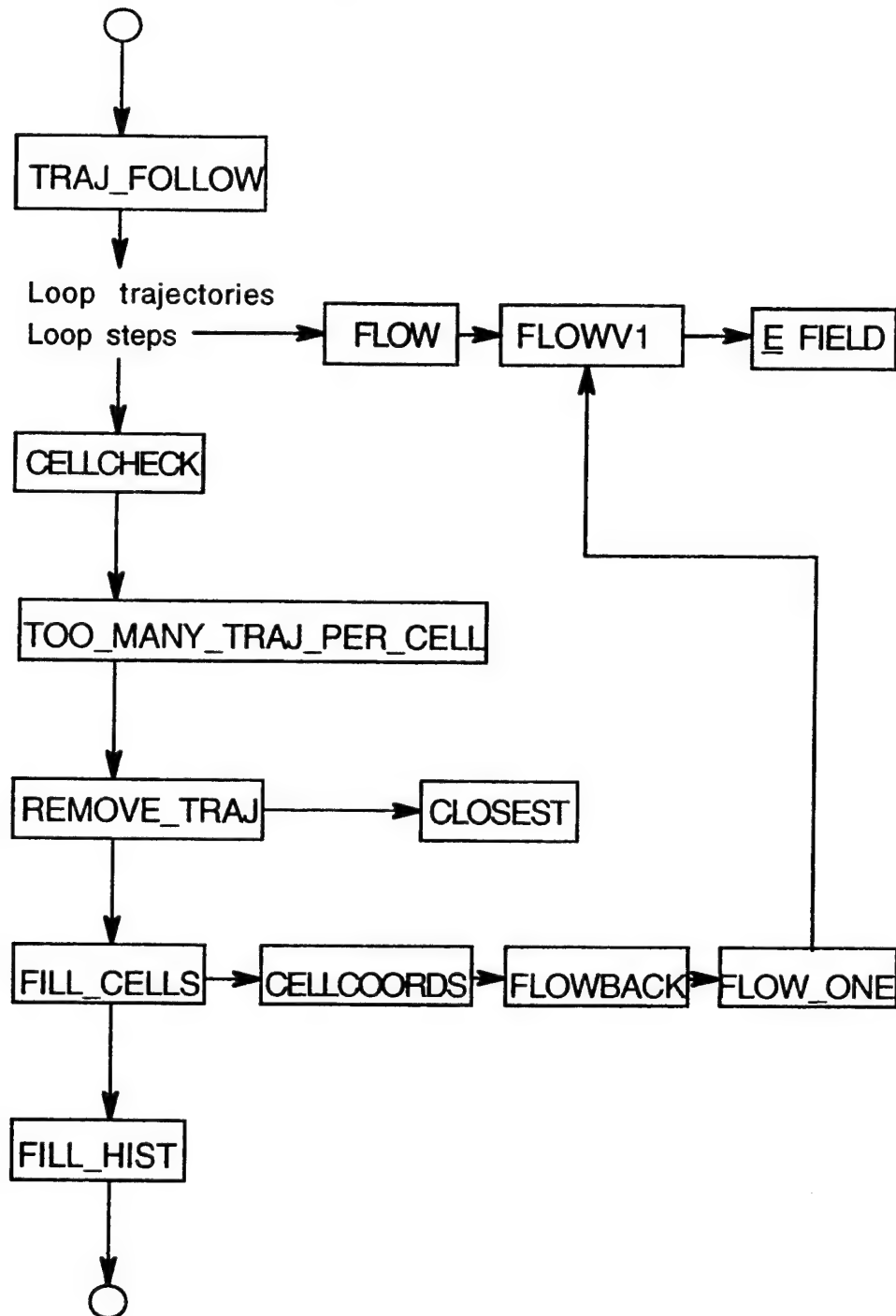


Figure 2. Block diagram showing how many trajectories to select, how many plasma flux tubes to follow, and where the flux tubes should be placed initially.

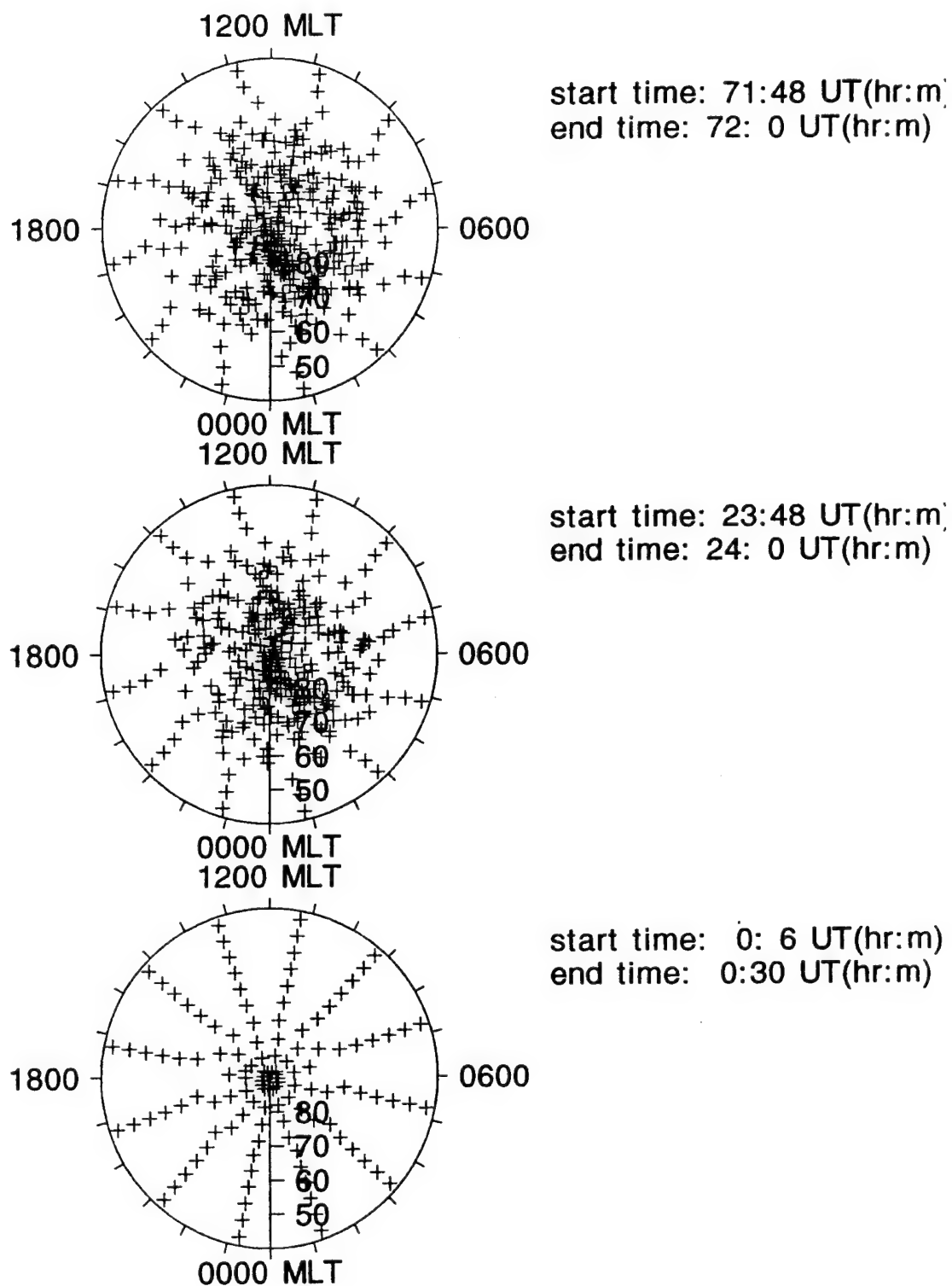


Figure 3. Flux tube locations at the start of the simulation (bottom panel), after 1 day (middle panel), and after 3 days (top panel) for $K_p = 1$.

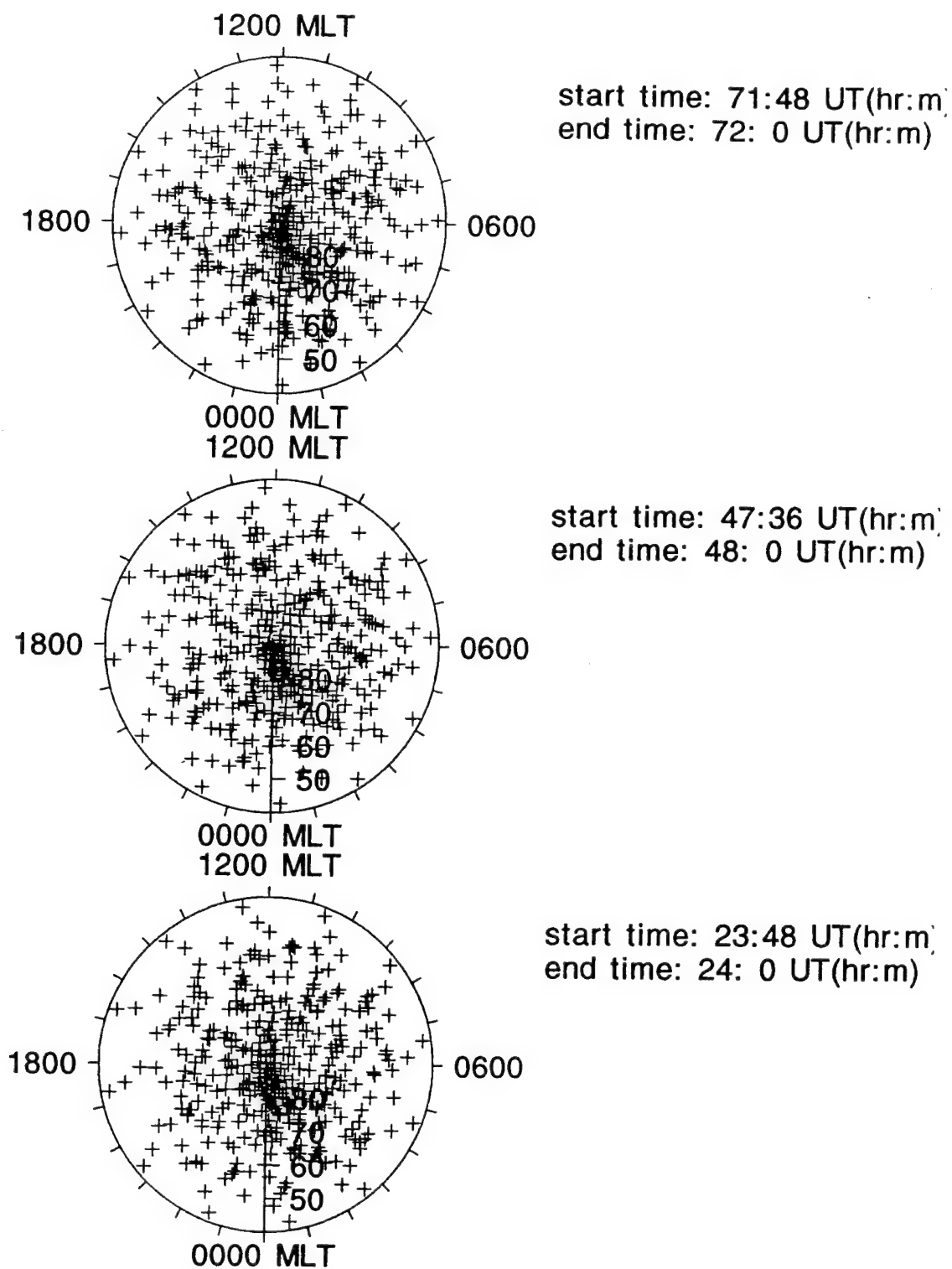
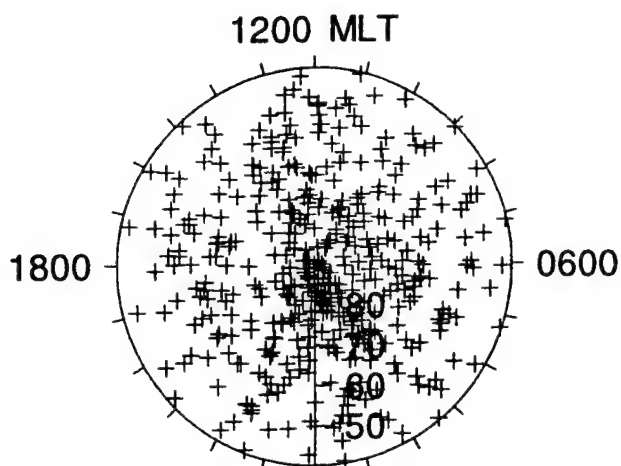
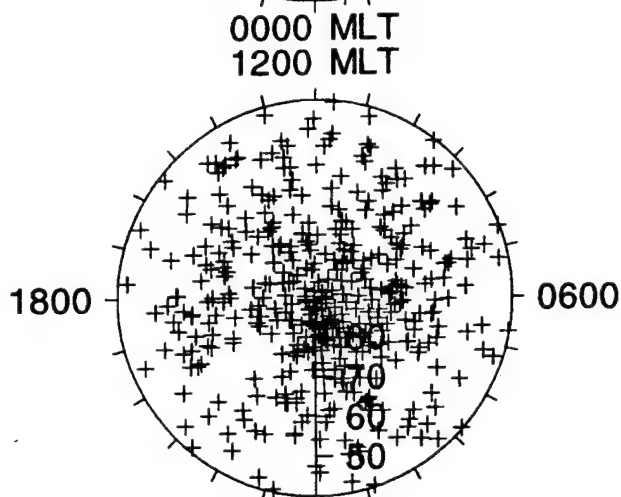


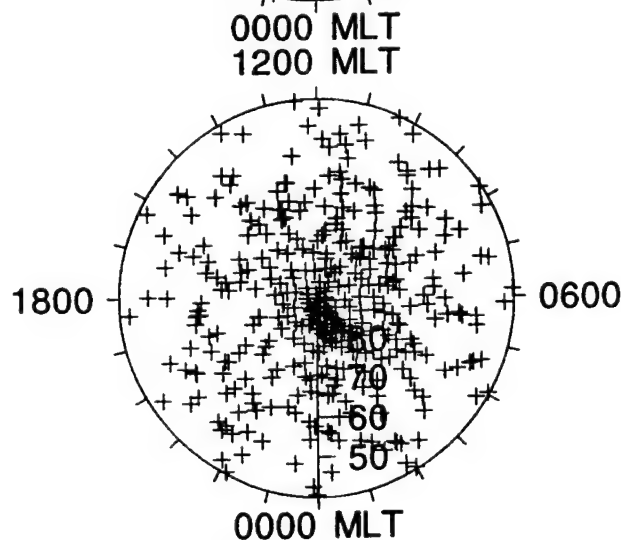
Figure 4. Flux tube locations at the start of the simulation (bottom panel), after 1 day (middle panel), and after 3 days (top panel) for $K_p = 4$.



start time: 71:48 UT(hr:m)
end time: 72: 0 UT(hr:m)



start time: 47:36 UT(hr:m)
end time: 48: 0 UT(hr:m)



start time: 23:48 UT(hr:m)
end time: 24: 0 UT(hr:m)

Figure 5. Flux tube locations at the start of the simulation (bottom panel), after 1 day (middle panel), and after 3 days (top panel) for Kp = 7.

5. NUMERICAL SOLUTION

For the mid-high latitude domain, the diffusion and thermal conduction equations are solved as a function of altitude for convecting plasma flux tubes. In our comprehensive ionospheric model, a fixed spatial step is used from the bottom to the top boundary (100-800 km). Also, three ions (NO^+ , O_2^+ , O^+) are assumed to be major ions, which means the three coupled diffusion equations must be solved simultaneously. However, experience has shown that NO^+ and O^+ are the dominant ions in the altitude region where diffusion is important, and a 2-ion code is computationally more efficient than a 3-ion code. Hence, the IFM is based on a two "major ion" formulation in the F-region. Also, a small spatial step is generally needed in the E-region to resolve the peak, but a larger spatial step can be used in the F-region because the peak is much broader. Again, for computational efficiency, the IFM formulation is divided into separate E and F regions.

The IFM solution procedure is as follows. An altitude is selected which defines the separation between the E and F regions (≈ 130 km). In the E-region a 4 km spatial step is used, while in the F-region the spatial step is larger (10-20 km), as shown in Figure 6. The E and F region density equations are solved as a function of time with a 10 - 100 second time step for convecting flux tubes. Every 15 minutes, the required inputs, the associated parameters, and the plasma temperatures are calculated. The sequence of these calculations is shown in Figure 7. Subroutine ONE first calls routines that calculate altitude profiles for the neutral densities and temperature (ATMOS), the electron temperature (TE), the ion temperature (TI), diffusion coefficients (DIFF), chemical reactions (CHEM), photoionization (PHOTO and SOLAR), production due to resonantly scattered solar radiation (RESONANT) and auroral precipitation (AURORA), the bottom boundary conditions (BC), and the wind-induced vertical ion drift (WIND). With altitude profiles of these parameters, ONE then calculates the coefficients that appear in the partial differential equations that describe the spatial and temporal variation of the ion densities.

5.1. E-Region

In the above solution procedure, the E-region densities are obtained by assuming chemical equilibrium (equation 1), but all four ions are allowed to have comparable densities. The resulting four coupled nonlinear equations are solved by first expanding the coupling and nonlinear terms in a Taylor series in time and then by iterating to a solution from an initial guess. The iteration can be done separately at each altitude step.

5.2. F-Region

The F-region densities are obtained from diffusion equations for the major ions NO^+ and O^+ . These diffusion equations are derived by substituting the momentum equations (4 and 5) into the continuity equations (2 and 3) taking into account charge neutrality (6) and charge conservation (7). Next, all of the coupling and nonlinear terms in the two diffusion equations are expanded in a Taylor time-series, but the algebra is considerably more involved than that described above for the E-region solution because of the density derivative terms. Appendix A gives the resulting diffusion equations after they have been "linearized in time." This set of coupled, second-order, parabolic, partial differential equations is solved with a completely implicit numerical technique, as shown symbolically in Figure 8 [FREGION2]. This numerical solution requires taking derivatives [GRAD], setting up coefficients [ADCOEF, RECOEF, CBCOEF], and applying boundary

conditions [TOPDEN] before the double tridiagonal matrix is solved. The bottom boundary conditions for the F-region solution is obtained from the top of the E-region. After the NO⁺ and O⁺ density profiles are calculated, the N₂⁺ and O₂⁺ density profiles are calculated assuming they are minor ions in chemical equilibrium (equation 1).

Figure 9 shows an example of a complete density solution with different solution procedures and spatial steps in the E and F regions. The spaces in the profiles are intentional to more clearly show the two regions. For this example, the altitude separating the E and F regions is 180 km.

5.3. Temperatures

The numerical solution for T_i is straightforward, since a local thermal balance is assumed at all altitudes (equation 8). In this case, the equation for T_i is algebraic.

The numerical solution for T_e is more involved because the electron energy equation is a nonlinear, second order, partial differential equation (i.e., equation 9). To improve numerical stability, the altitude domain is divided into a lower domain, where thermal conduction is negligible and a local thermal balance exists, and an upper domain, where the complete energy equation is solved. In the lower altitude domain, T_e is obtained from the resulting nonlinear algebraic equation by iterating from an initial guess. In the upper altitude domain, equation 9 is solved by introducing the variable $\theta = T_e^{7/2}$, by expanding all nonlinear terms in a Taylor time-series, by replacing all derivatives with finite difference expressions, and by inverting the resulting matrix with a standard tridiagonal technique (cf. Schunk, 1988a). The bottom boundary condition is obtained from the T_e value at the top of the lower altitude domain. At the top boundary, a downward thermal conduction flux is specified.

Again, for numerical stability reasons, the spatial grid on which the electron energy equation is solved is decoupled from the spatial grid on which the diffusion equations are solved. This is for two basic reasons. First, the altitude separating the E and F regions, Z_{EF} , may not coincide with the altitude up to which a local thermal balance applies, Z_c . Also, because the density and temperature gradients have different spatial scales, computational efficiency dictates different step sizes for the diffusion and energy equations.

Figure 10 shows a typical spatial grid for the density code and four possible spatial grids for the T_e code. For the density code, a 20 km step is used in the F-region and a 4 km step in the E-region. For the T_e code, the first example is for a 20 km step at all altitudes and Z_c below Z_{EF} ; the second example is for $\Delta Z = 20$ km and Z_c above Z_{EF} ; the third and fourth examples are for $\Delta Z = 4$ km and Z_c below and above Z_{EF} , respectively. Finally, Figure 11 shows T_e and T_i profiles for a case where a 4 km spatial step is necessary in the T_e code at altitudes above Z_c because of a rapid increase in T_e with altitude. The spatial steps in the corresponding density code are 4 km in the E-region and 20 km in the F-region.

5.4. H⁺ Formulation

The IFM has a relatively simple prescription for calculating H⁺ densities. The

algorithm developed is based on information obtained from both satellite data and numerous polar wind studies (cf. Schunk, 1988b; and references therein). In constructing the model, account was taken of the fact that below about 500-700 km, H⁺ is a minor ion in chemical equilibrium at all latitudes and longitudes. Since the main source and loss of H⁺ stems from the accidentally resonant charge exchange reaction,



the chemical equilibrium expression for H⁺ becomes

$$N(\text{H}^+) = 1.13(T_n / T_i)^{1/2} N(\text{H})N(\text{O}^+) / N(\text{O}) \quad (11)$$

Therefore, at the altitudes where this expression is valid, H⁺ can be obtained using the MSIS atmospheric model values for N(H), N(O), and T_n in combination with the IFM values for N(O⁺) and T_i. At altitudes above the domain where chemical equilibrium prevails, different prescriptions are used in different latitude regions. The latitude regions are below 55°, 55° to 65°, and above 65° magnetic latitude.

At low-mid latitudes (<55°), the H⁺ altitude distribution changes quickly from chemical equilibrium to diffusive equilibrium. However, as it turns out, when H⁺ is a minor ion the chemical equilibrium and diffusive equilibrium scale heights are nearly identical. Therefore, with a negligible error, the H⁺ density can be calculated with the chemical equilibrium formula (11) up to an altitude where N(H⁺) = N(O⁺). Above this transition altitude, the H⁺ density decreases exponentially according to the following diffusive equilibrium formula,

$$N(\text{H}^+) = N_B(\text{H}^+) \exp[(z_B - z) / H_i] \quad (12)$$

$$H_i = k(T_e + T_i) / M(\text{H}^+)g \quad (13)$$

where N_B(H⁺) is the bottom boundary value obtained from the top of the chemical equilibrium domain. However, in order to obtain a smooth transition from the growing to the decreasing exponential solutions, they are combined over a small altitude region near the transition altitude.

At high latitudes (>65°), the geomagnetic field lines are 'open' and, as a consequence, H⁺ is in a continual state of outflow. Both model studies and measurements indicate that the H⁺ escape flux is saturated and that H⁺ remains a minor ion to high altitudes (≈3000 km). In such a situation, the H⁺ density first increases with altitude in the low-altitude chemical equilibrium domain, reaches a peak, and then decreases with altitude with a scale height that is equal to the O⁺ scale height. An examination of a number of polar wind studies indicates that the H⁺ peak density is approximately 2% of the O⁺ density at the peak altitude (cf. Schunk, 1988b). Therefore, the simple prescription used in the IFM to calculate H⁺ density profiles at high latitudes is as follows. Chemical equilibrium is

assumed up to an altitude where $N(H^+) = 0.02N(O^+)$. At high altitudes, the H^+ scale height is set equal to the O^+ scale height,

$$H(H^+) = H(O^+) = k(T_e + T_i) / M(O^+)g \quad (14)$$

The high and low altitude H^+ density segments are then connected with a parabolic profile over a 50 km transition region. It should be noted that the resulting H^+ density profiles are very similar to those obtained in model studies of the polar wind.

The latitudinal region $55^\circ - 65^\circ$ corresponds to the light ion trough, wherein the H^+ density undergoes a transition from diffusive equilibrium at 55° to continual outflow at 65° . At a fixed altitude, a satellite traversing this region from low to high latitudes typically measures a constant O^+ density, but an H^+ density that decreases logarithmically due to the increasing importance of H^+ outflow (see Figure 12). With allowance for this additional feature, the prescription used to calculate H^+ density profiles in the $55^\circ - 65^\circ$ latitude domain is very similar to that used at high latitudes. Specifically, the chemical equilibrium formula (11) is used up to an altitude where $N(H^+) = (\text{factor}) \times N(O^+)$. The factor varies logarithmically with magnetic latitude from 1.0 at 55° to 0.02 at 65° . This basically determines the H^+ peak density and height. At high altitudes, the H^+ scale height is set equal to the O^+ scale height. Finally, the high and low altitude H^+ density segments are connected with a parabolic profile over a 50 km transition region. This latter step determines the exact values for the H^+ peak density and height.

Figure 13 shows typical H^+ and O^+ density profiles obtained from the IFM at different latitudes. The geophysical parameters are for summer daytime conditions, and the latitudes are along the noon magnetic meridian at 54° , 60° , 64° , and 68° (from left to right). The latitudes correspond to one below the light ion trough, two in the light ion trough, and one at high latitudes. These latitudes cover all three domains in the H^+ formulation and, hence, the H^+ density profiles in Figure 13 are representative of what is obtained from the IFM.

5.5. Equatorial Model Implementation

As already described, the equatorial model developed by Anderson [1973] and recently validated by Preble et al. [1994] is the basis for the IFM equatorial F-region model. Its implementation into the IFM required the following steps:

1. The Anderson model had to be upgraded from a single longitude to a global model.
2. The Anderson model time sequencing had to be modified such that global ionospheric "snapshots" could be acquired every 1 hour and, if requested, a forecast as short as 1 hour could be run.
3. An entirely new capability of "hot starting" the Anderson model had to be developed.
4. This required the development of a module that creates the hot start database, if required.

5. An E-region had to be added to the Anderson F-region O⁺ model.

The equatorial model is interfaced with IFM through a single call to subroutine IFM_EQU.f. This subroutine carries out various operations which are shown in block diagram form in Figure 14. The first of which is to interface to the run conditions already defined by the IFM.SETUP file and augmented by the EQU.SETUP. At this point in the sequence, the equatorial module can return (in the event of no equatorial region being needed); compute a cold start; or begin with a hot start. The hot start is a set of ascii datasets, one per longitude, that contain initialization of coefficients for the Anderson model. These are more extensive than just ionospheric parameters, ie, density, temperature, etc. They need to be generated by running the Anderson model in the GET_HOT_START mode (See Figure 14). Once a hot start is available, (note if a cold start is required the subroutine GET_HOT_START is run first to obtain the corresponding hot start conditions), the subroutine EQU_F_REGION is run (see Figure 14). This generates a database of field line O⁺ densities at the required Latitudes, MLT's and UT's. However, this database has an uneven altitude distribution, hence, a further stage of interpolation is required. EQU_ALT_INT carries out this interpolation which is a linear interpolation, on log₁₀ (O⁺) and linear altitude (see Figure 14). These altitude profiles are then transferred to the final IFM output database as O⁺ densities.

The final stage of the equatorial model is to add an E-region to the above F-region. In Figure 14 this is shown as a call to subroutine EQU_E_REGION. This subroutine uses the IFM mid and high latitude E region formulation and is run in the same manner as already described in the preceding sections on the E-region in the mid-high latitude formulation. This model then adds the molecular ions to the O⁺ in the final IFM output database.

The merging of the equatorial model output with the high-mid latitude model output occurs as the data is written to the IFM output database. This is done within the EQU_ALT_INT.f and IFM_E_REGION.f subroutines. There is no requirement for a final merging program to match the various model outputs into the final IFM output database.

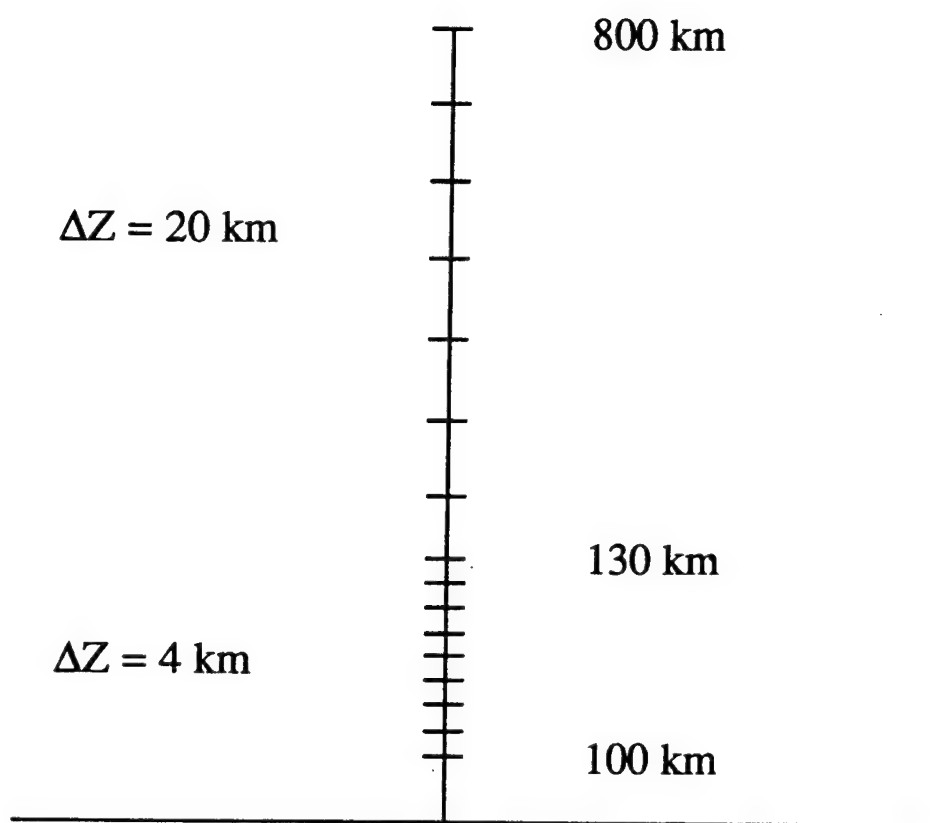


Figure 6. The IFM is based on different altitude grid spacings in the E and F regions.

ALTITUDE PARAMETERS

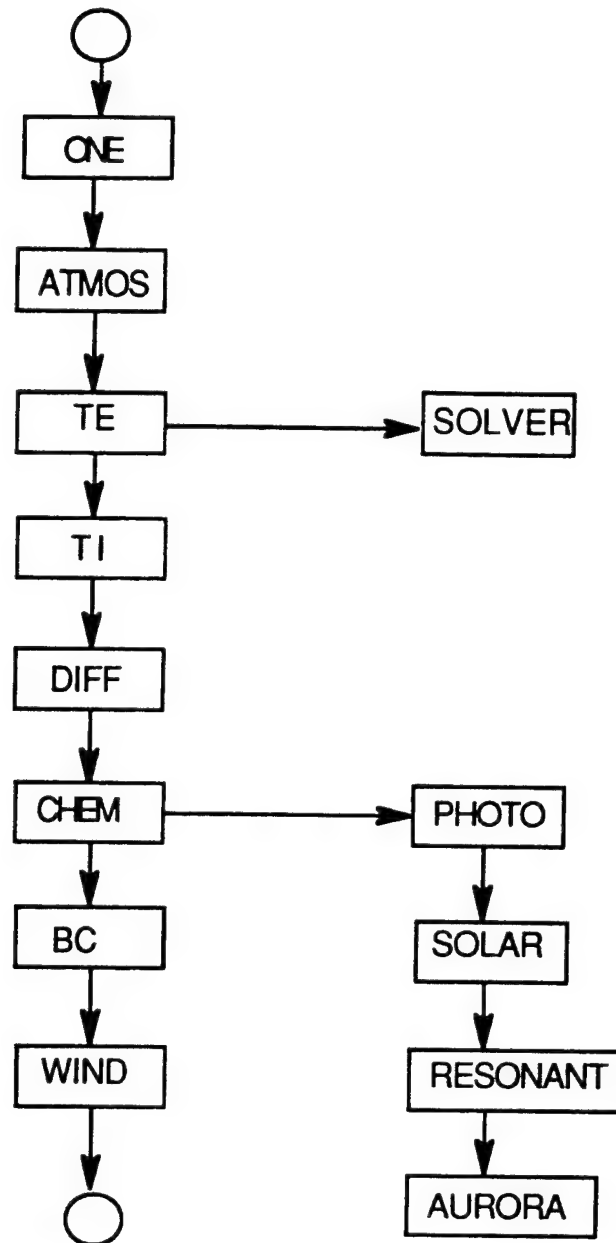


Figure 7. Block diagram showing the sequence of calculations done at 15-minute intervals. These calculations provide the required inputs, associated parameters, and plasma temperatures needed by the density solver.

Numerical Solution

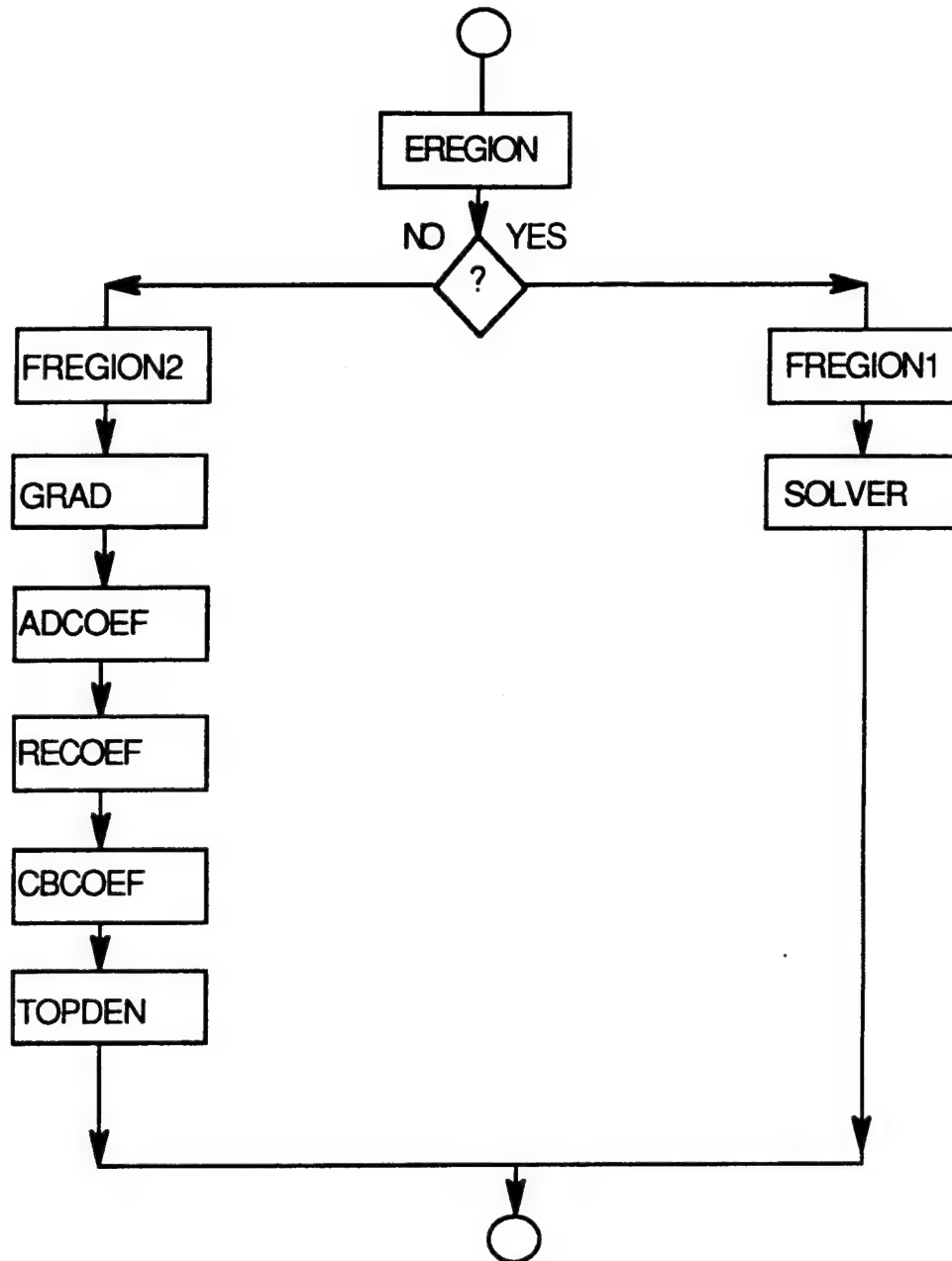


Figure 8. Block diagram showing the sequence of subroutine calls needed to obtain a numerical solution of the ion diffusion equations.

Solar Maximum-Winter

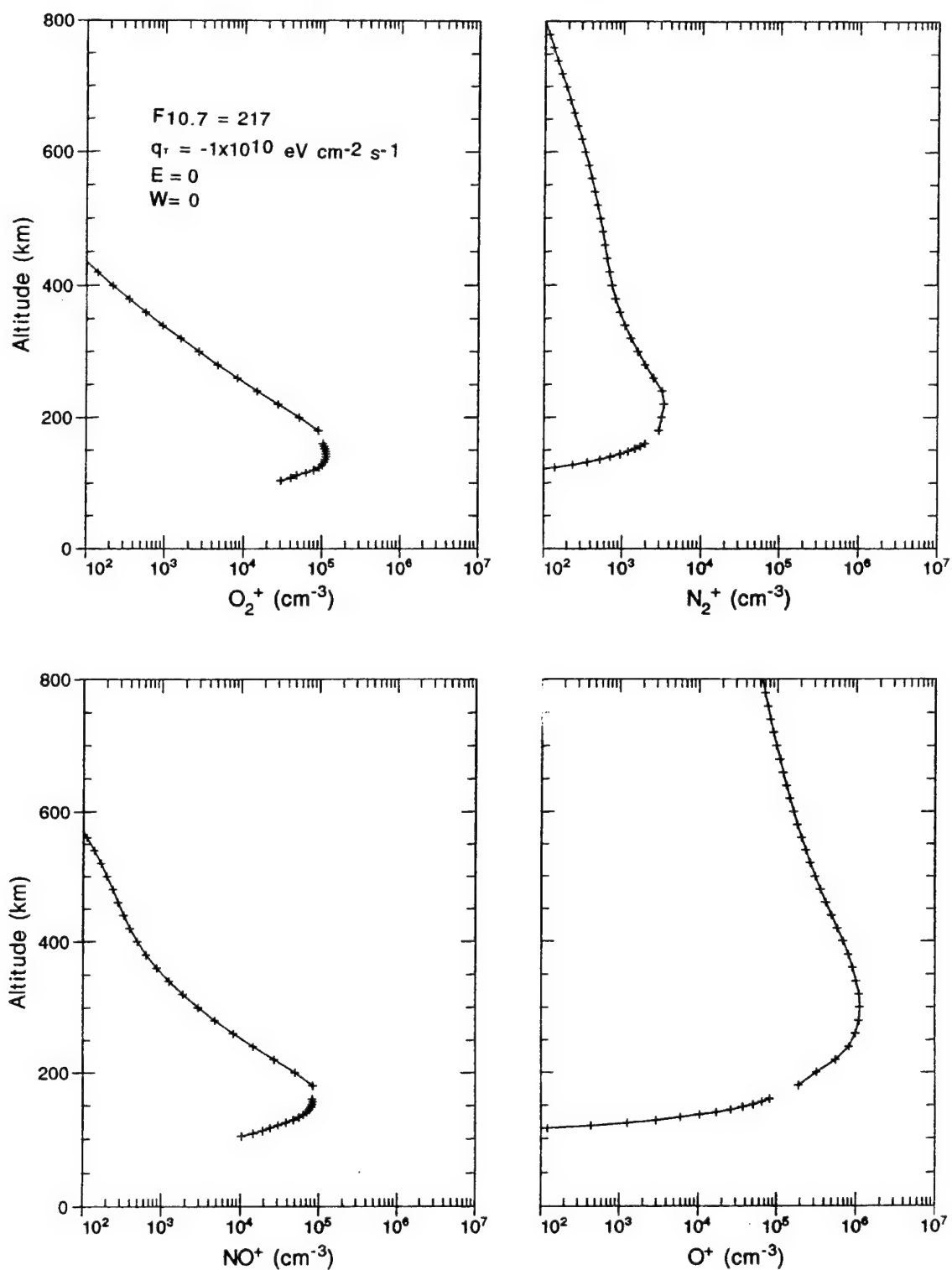
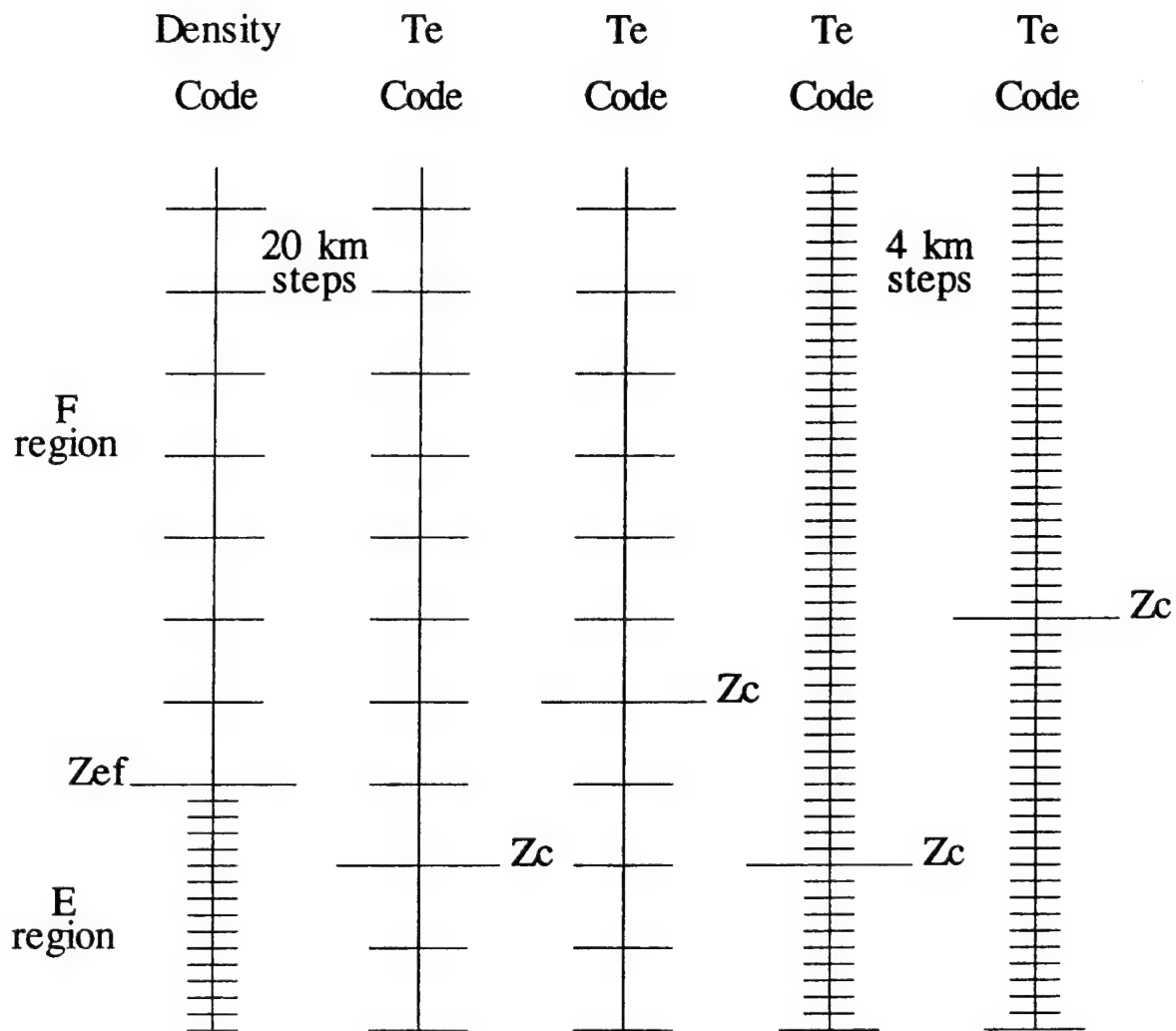


Figure 9. Altitude profiles of the molecular and oxygen ion densities for daytime steady state conditions. The density profiles were obtained with different solution procedures in the E and F regions.

DENSITY and Te GRIDS DECOUPLED

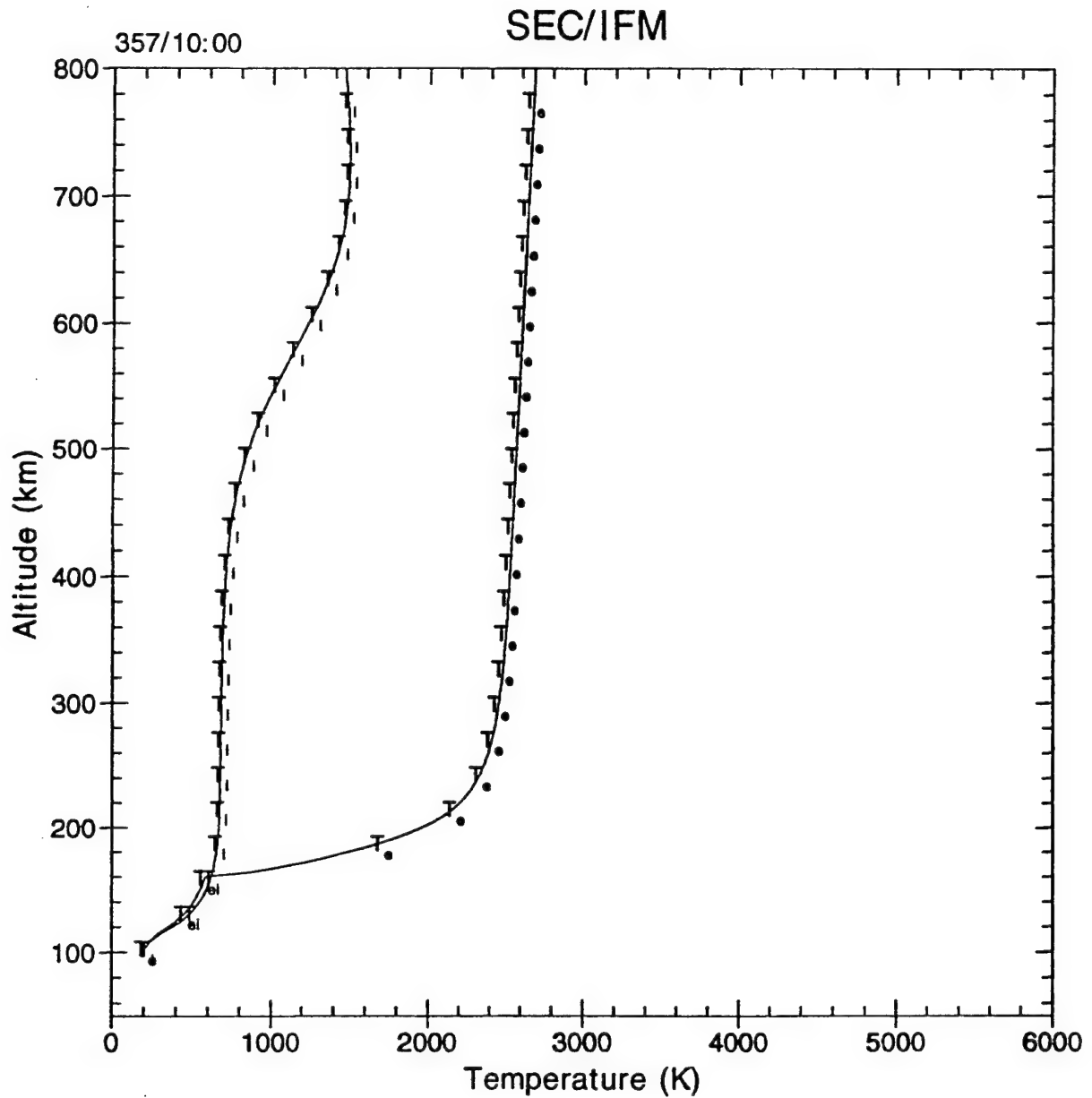


Zef: E region - F region interface

Zc: Heating = Cooling below this altitude

Figure 10. Schematic diagram showing the decoupling of the spatial grids used in the density and electron temperature solvers.

$$\Delta Z = 4 \text{ km}$$



year 1987, f10.7 70.0, f10.7a 70.0, ap 4.0, kp 1.0
 Trajectory SN 1, Step 20, NmF2 0.937E+04, HmF2 248.
 MLT 16.85, Latitude 71.2

Figure 11. Altitude profiles of the ion and electron temperatures at a location and time when a 4 km spatial step was needed because of the steep electron temperature gradient.

MID-HIGH LATITUDE TRANSITION

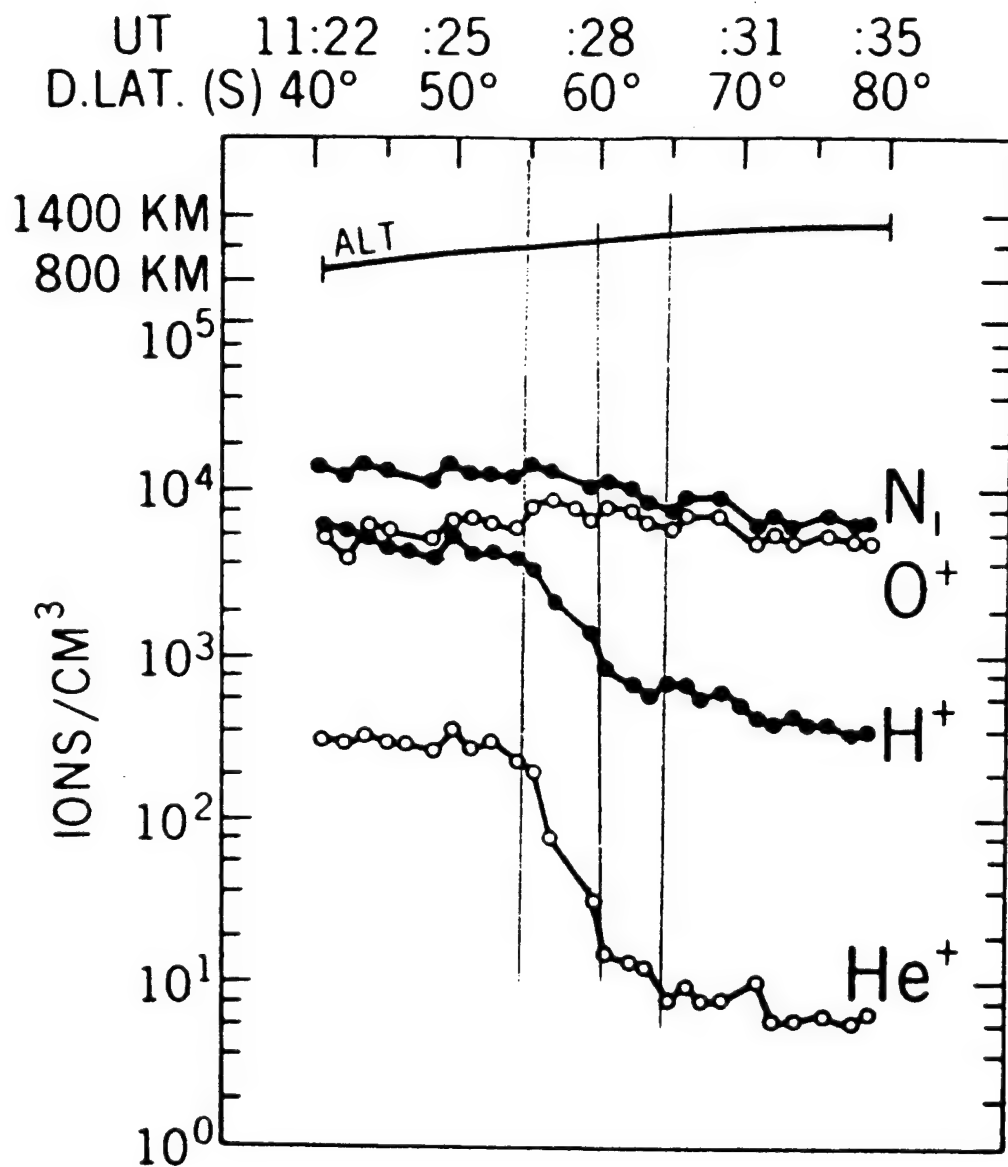
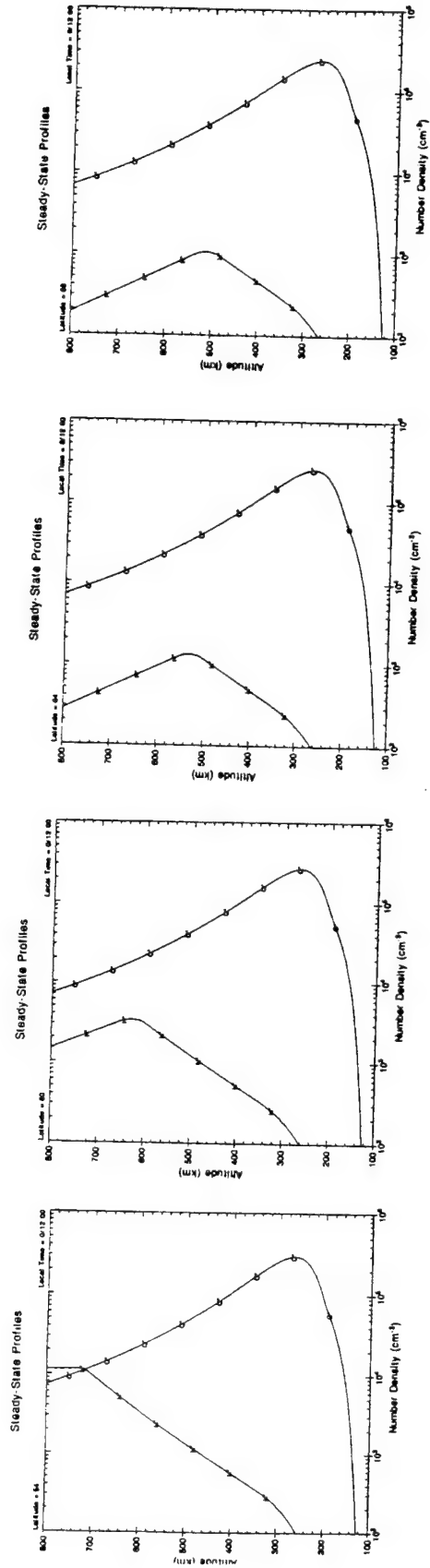


Figure 12. Plasma ion measurements from the ISIS satellite.



LATITUDE VARIATION

Figure 13. H⁺ and O⁺ density profiles along the noon magnetic meridian at latitudes of 54°, 60°, 64°, and 68° (from left to right).

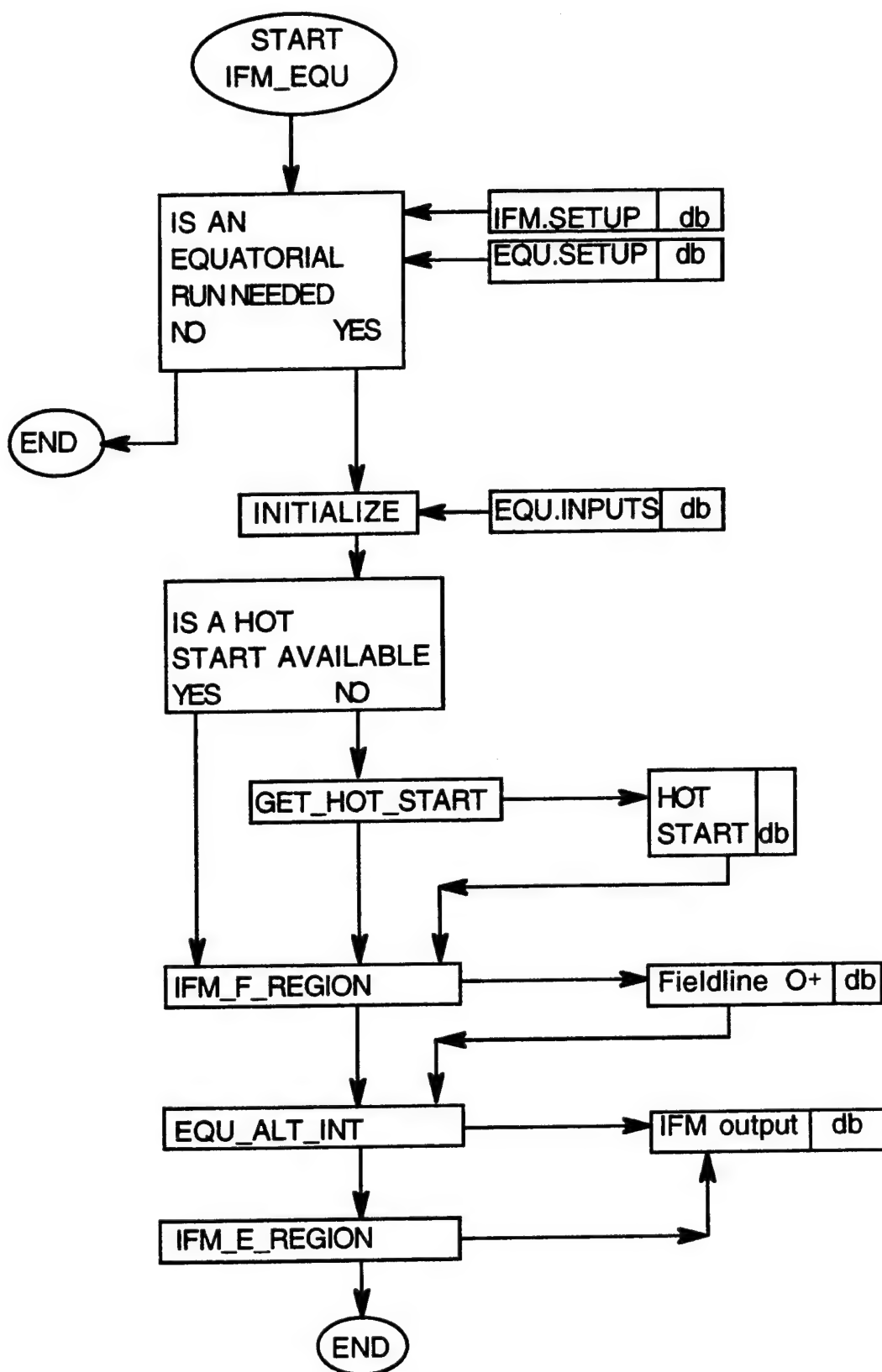


Figure 14. Block diagram showing the logical steps needed to run the equatorial part of the IFM.

6. IFM VALIDATION

The current version of the IFM has been validated at three different levels. The first involves validating the physics and chemistry upon which the numerical model is based. The next is verifying that the streamlined model is consistent with the comprehensive ionospheric model. The last validation concerns comparisons of model predictions with the kind of data that will be available at the Space Forecast Center. In the subsections that follow, our validation efforts in these three areas will be briefly discussed.

6.1. Physics and Chemistry

The physics and chemistry contained in the comprehensive ionospheric model have been validated over a 14 year period and the results have been published in a series of papers. These papers are listed in Appendix C and for each paper highlights are given in bullet form. The appendix only covers the validation efforts concerning mid and high latitude data. However, the Anderson model of the equatorial ionosphere has also been validated over the years and it is clear that the physics and chemistry contained in that model are correct (cf. Preble et al, 1994; and references therein).

With regard to the mid and high latitude domains, Appendix C shows that numerous satellites and radars have been involved in various aspects of our validation. Over the years, we have used data from five satellites (AE-C, DMSP F2 & F4, NOAA-6, DE-2), four incoherent scatter radars (Millstone Hill, Chatanika, EISCAT, Arecibo), two coherent radars, and about 50 ionosondes spread around the world. Note that 41 ionosondes were used in one study alone and that 12 Soviet ionosondes were used in another study. Note also that the validation efforts covered different solar cycle (maximum to minimum), seasonal (winter, equinox, summer), and magnetic activity (high, medium, low) conditions. Diurnal variations were studied as well as longitudinal effects. Finally, note that the validations involved the model predictions for N_mF_2 , h_mF_2 , the electron densities at different altitudes, the ion composition, and the electron and ion temperatures.

The main conclusion to be drawn from the various validation studies that we, and others, have conducted over the years is that critical inputs are needed in each of the three latitudinal domain. If these inputs are known, the ionospheric model predictions are very reliable. The critical inputs are the plasma convection and particle precipitation patterns at high latitudes, the thermospheric wind at mid-latitudes, and the electrodynamic drift at low latitudes.

6.2. Streamlined Versus Comprehensive Model

As part of the PRISM development effort, our comprehensive ionospheric model was run 54 times in order to produce background ionospheres in the event that real-time data were not available to drive PRISM. The 54 cases corresponded to 3 levels of solar activity, 3 seasons, 3 levels of geomagnetic activity, and 2 background plasma convection patterns (IMF By positive and negative). The 54 simulations displayed a wide range of ionospheric features, including tongues of ionization, polar holes, nightside and dayside ionization troughs, auroral ionization enhancements, elevated sunlit regions, and ion and electron temperature hot spots. The simulations also showed how these features varied with altitude, latitude, longitude and universal time.

In verifying that the streamlined and comprehensive models produce the same results,

we repeated many of these 54 cases and, indeed, obtained very similar results. An exact agreement was not expected because the streamlined IFM model was run with the MSIS wind (rather than the simple prescription used in the original 54 simulations) and because the solar EUV fluxes and O⁺-O collision frequency were modified according to recommendations from the PRIMO community. Figures 15 to 18 show four representative IFM simulations for the following geophysical conditions:

<u>Case 1</u>		
Solar Minimum	(F10.7 = 70)	
Winter	(Day 357)	
Low Activity	(Kp = 1)	
<u>Case 2</u>		
Solar Maximum	(F10.7 = 210)	
Winter	(Day 357)	
Low Activity	(Kp = 1)	
<u>Case 3</u>		
Solar Maximum	(F10.7 = 210)	
Winter	(Day 357)	
High Activity	(Kp = 6)	
<u>Case 4</u>		
Solar Minimum	(F10.7 = 70)	
Winter	(Day 357)	
High Activity	(Kp = 6)	

All four cases are for the Northern Hemisphere and magnetic latitudes from 40° to the pole. For cases 1-3, snapshots of N(O⁺) at 300 km, N(NO⁺) at 300 km, and h_mF₂ are shown at 0 UT. For case 4, N_mF₂, h_mF₂, N_e at 140 km, N_e at 800 km, T_i at 500 km, and T_e at 230 km, are shown at both 0700 and 1900 UT.

For solar minimum, winter, and low magnetic activity (Figure 15a-c), the IFM simulation displays all of the features that are expected, based on the corresponding simulation conducted with the comprehensive ionospheric model. At 300 km, the O⁺ density distribution exhibits elevated densities on the dayside, a polar hole, elevated densities in the nocturnal auroral oval, and a morning mid-latitude trough. The NO⁺ density distribution displays similar (not identical) features, but at 300 km the values are considerably lower than those of O⁺, as expected for low magnetic activity. At mid-latitudes, h_mF₂ is depressed on the dayside and elevated on the nightside, which is in agreement with the expected behavior due to the transpolar thermospheric wind. If the solar cycle level is changed from minimum to maximum keeping all of the other parameters the same (Figures 16a-c), the O⁺ and NO⁺ density features are similar but the density levels are higher, which is again what is expected. Likewise, the h_mF₂ values at solar maximum are considerably higher than those at solar minimum.

The simulations that are shown in Figures 17 and 18 were run with a Volland (1978) asymmetric convection pattern with enhanced flow in the dusk section. Because of this asymmetry and because of the large convection speeds associated with Kp = 6, the resulting ionospheric features are significantly different than those obtained for Kp = 1. Comparing the corresponding solar maximum winter cases for Kp = 1 (Figures 16a-c) and

$K_p = 6$ (Figures 17a-c) several important differences are evident. First, an O^+ hole and a corresponding NO^+ density buildup appear in the dusk sector coincident with the strong convection cell. Also note that the polar region extends to lower latitudes for $K_p = 6$, which results in lower dayside densities. Finally, note that both high (500 km) and low (150 km) $h_m F_2$ values are coincident with the strong convection cell in the dusk sector.

The $K_p = 6$ results for solar minimum are shown in Figures 18a-f, where snapshots of $N_m F_2$, $h_m F_2$, N_e at 140 km, N_e at 800 km, T_i and T_e are displayed at 0700 and 1900 UT. These times correspond to the extreme locations of the terminator in the magnetic reference frame. The basic features shown in these figures are very similar to those obtained in a corresponding run of our comprehensive ionospheric model and the underlying physics is straightforward. The strong convection speeds in the dusk convection cell result in elevated ion temperatures due to ion-neutral frictional interactions. The enhanced T_i 's, in turn, cause a depletion in O^+ and an enhancement in NO^+ because of the temperature dependence of the $O^+ + N_2 \rightleftharpoons NO^+ + N$ reaction rate. The elevated T_i 's also produce enhanced T_e 's due to collisional coupling of the ions and electrons. However, the various density and temperature features are modulated by the motion of the terminator in the magnetic frame.

6.3. Observational Data

Ionospheric models are being compared with observations on both national and international levels in order to validate the models in application environments. As a result, well defined and quality controlled observation datasets are available against which the IFM can be compared. One of these comparison efforts is being carried out jointly by the NSF-CEDAR-PRIMO working group and the STEP-VIM working group.

PRIMO: Problems Related to Ionospheric Modelling and Observations is a community wide Ionospheric model and observation comparison initiative within the NSF-CEDAR program. These comparisons have been done for solar maximum and minimum, summer and winter for quiet geomagnetic conditions. The observations have come from the American sector (east coast) chain of digisonde stations. Comparisons of the IFM model results with observations from Millstone Hill and with the USU TDIM model are presented. The IFM agrees very well with both the observations and TDIM. At this time most of the difference between the IFM and TDIM results lie in using an oversimplified wind, which produces too large a midlatitude nighttime maintenance. This is especially the case during solar maximum. With the Hedin 90 wind model, this will be corrected. Figures 19a through 19d show the $N_m f_2$ comparisons of IFM (solid line), TDIM (long dashed line), and Millstone Hill observations (dotted line).

Summary of PRIMO Validation as of 1 August 1994.

Solar Minimum - Summer (Figure 19a)

Both $N_m F_2$ and $h_m F_2$ are in very good agreement with the observations. Indeed, the agreement appears to be better than with the TDIM.

Solar Minimum - Winter (Figure 19b)

$N_m F_2$ through daytime and early evening is good, but the predawn secondary

maximum is not well reproduced. H_mF_2 may be a little high (20 km). Comparable to TDIM results.

Solar Maximum - Summer (Figure 19c)

Daytime N_mF_2 and h_mF_2 are too high. The default wind has no downward drift on the dayside. Such a wind would lower the F-layer and reduce N_mF_2 . With a lower sunset N_mF_2 , an automatically improved nighttime N_mF_2 would be achieved. The Hedin-90 wind model, which will be delivered with the IFM, has a daytime wind and a lower nighttime wind.

Solar Maximum - Winter (Figure 19d)

Both daytime and nighttime N_mF_2 and h_mF_2 are too large. Nighttime wind is too strong. Replacing wind with Hedin-90 would reduce nighttime wind and introduce a daytime wind that would lower the layer and decrease the daytime N_mF_2 .

VIM: Validation of Ionospheric Models, is an international initiative designed to validate both physical and empirical ionospheric models. The VIM datasets were used for the solar maximum Millstone Hill data shown in Figure 19c and d. VIM also provides data at other locations and is representative of the data available at the AF Space Forecast Center to be used in driving ionospheric models.

EQUATORIAL: A very extensive validation of the Anderson model was carried out by Preble et al, [1994]. They used an extensive, high resolution dataset from the incoherent scatter radar at Jicamarca, Peru. The first version of the IFM is able to reproduce these results, verifying that the restructuring of the Anderson equatorial model within the IFM has been successful. Figure 20 compares the IFM (top panel) with the Preble et al., [1994] (bottom panel) O^+ density. These show the diurnal altitude variation of O^+ over Jicamarca for solar medium conditions $F_{10.7} = 128.7$. Preble et al., [1994] demonstrated that their model O^+ variations agree very well with the observed densities, hence validating that the IFM will do the same.

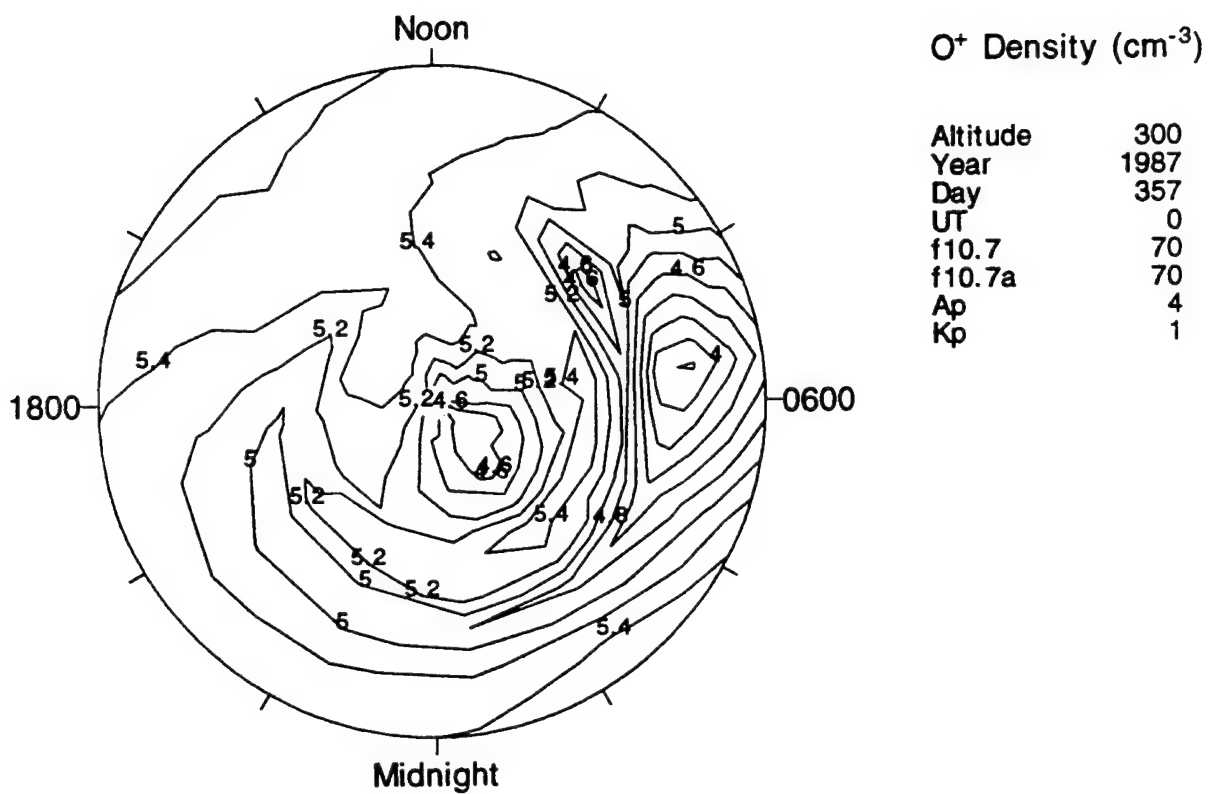


Figure 15a. Snapshot of the O⁺ density distribution at 300 km and 0 UT. The simulation represents solar minimum, winter, and low magnetic activity conditions.

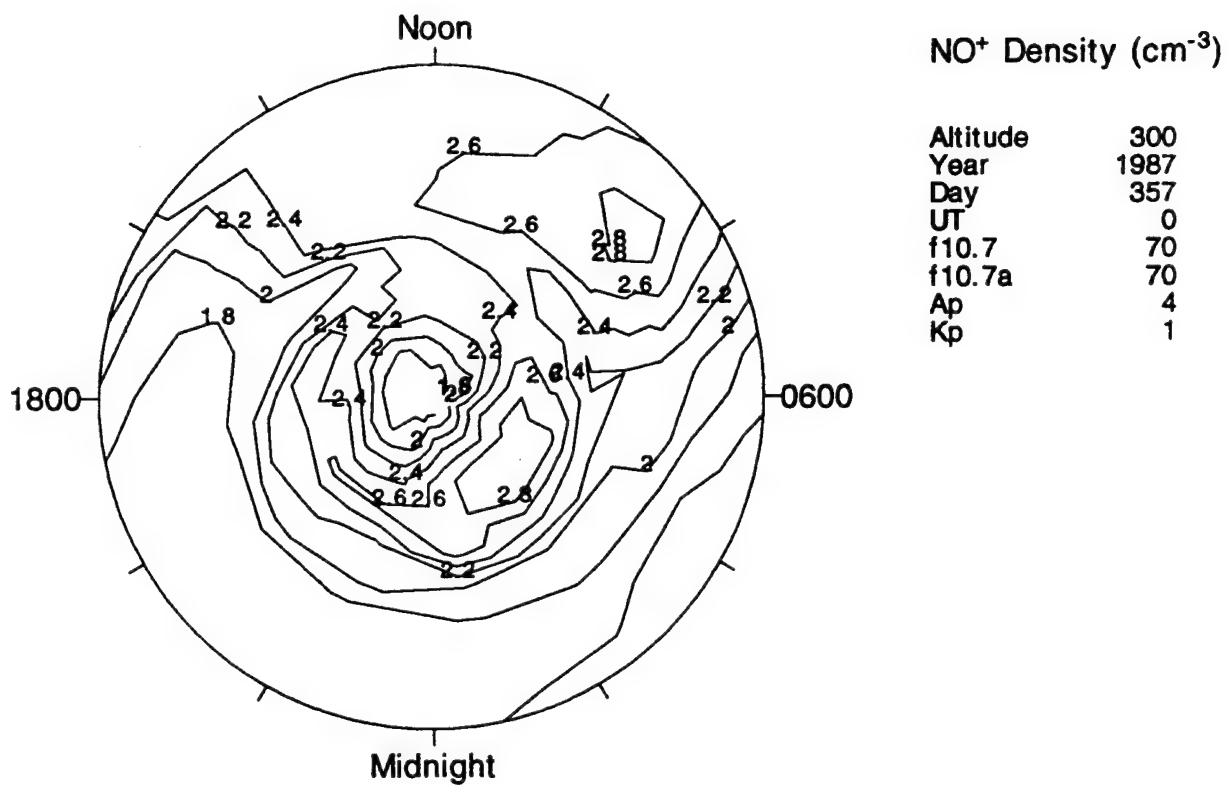


Figure 15b. Snapshot of the NO⁺ density distribution at 300 km and 0 UT. The conditions are the same as for Figure 15a.

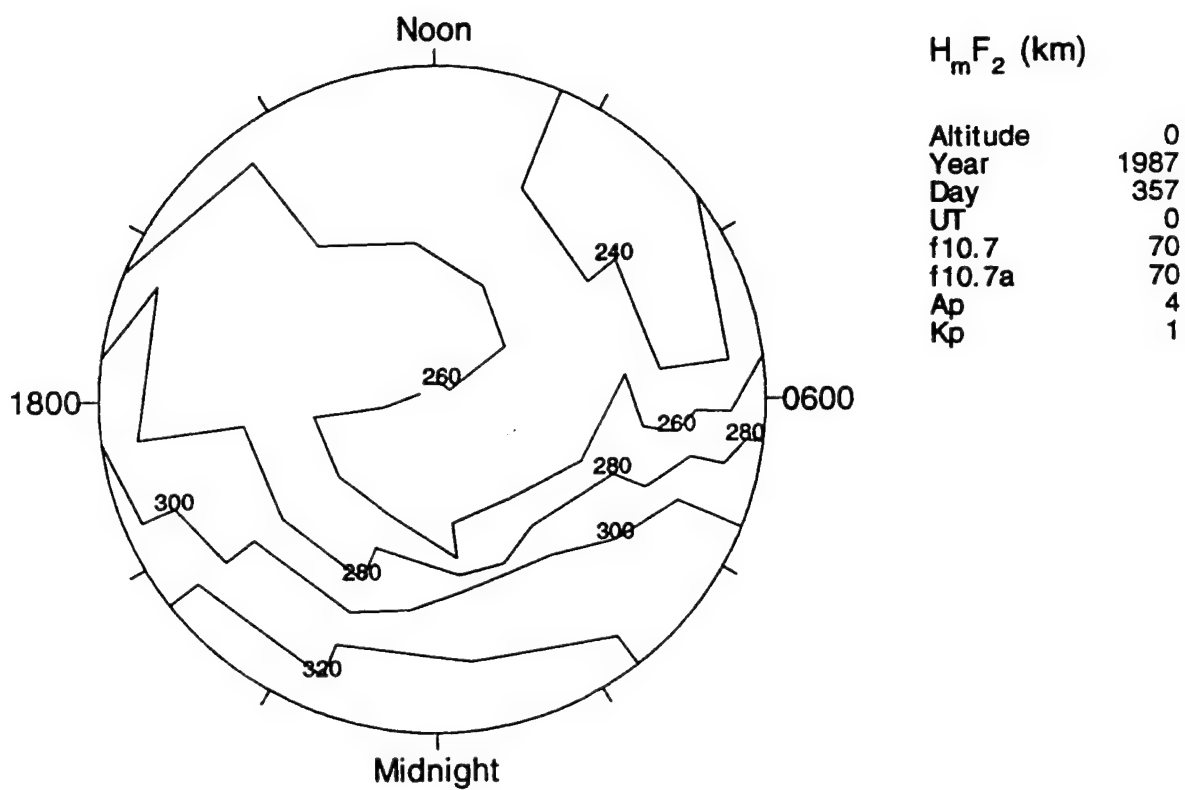


Figure 15c. Snapshot of $h_m F_2$ at 0 UT. The conditions are the same as for Figure 15a.

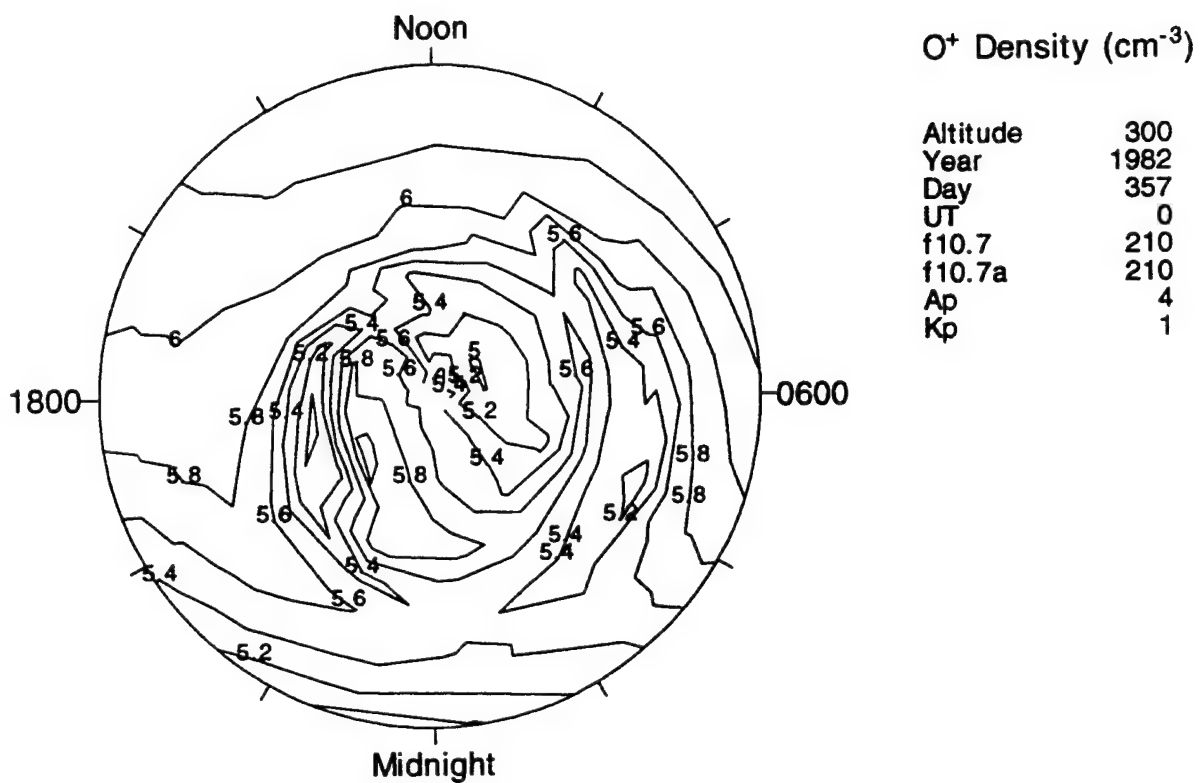


Figure 16a. Snapshot of the O⁺ density distribution at 300 km and 0 UT. The simulation represents solar maximum, winter, and low magnetic activity conditions.

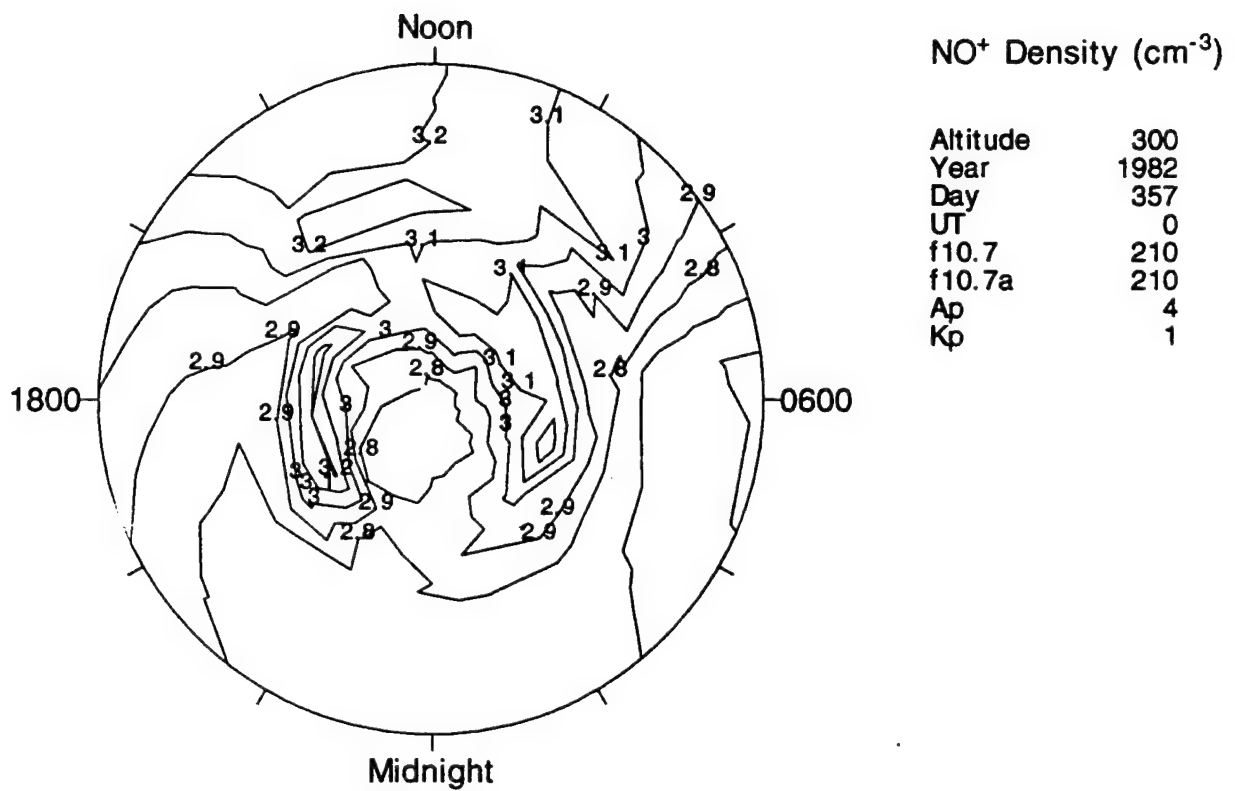


Figure 16b. Snapshot of the NO⁺ density distribution at 300 km and 0 UT. The conditions are the same as for Figure 16a.

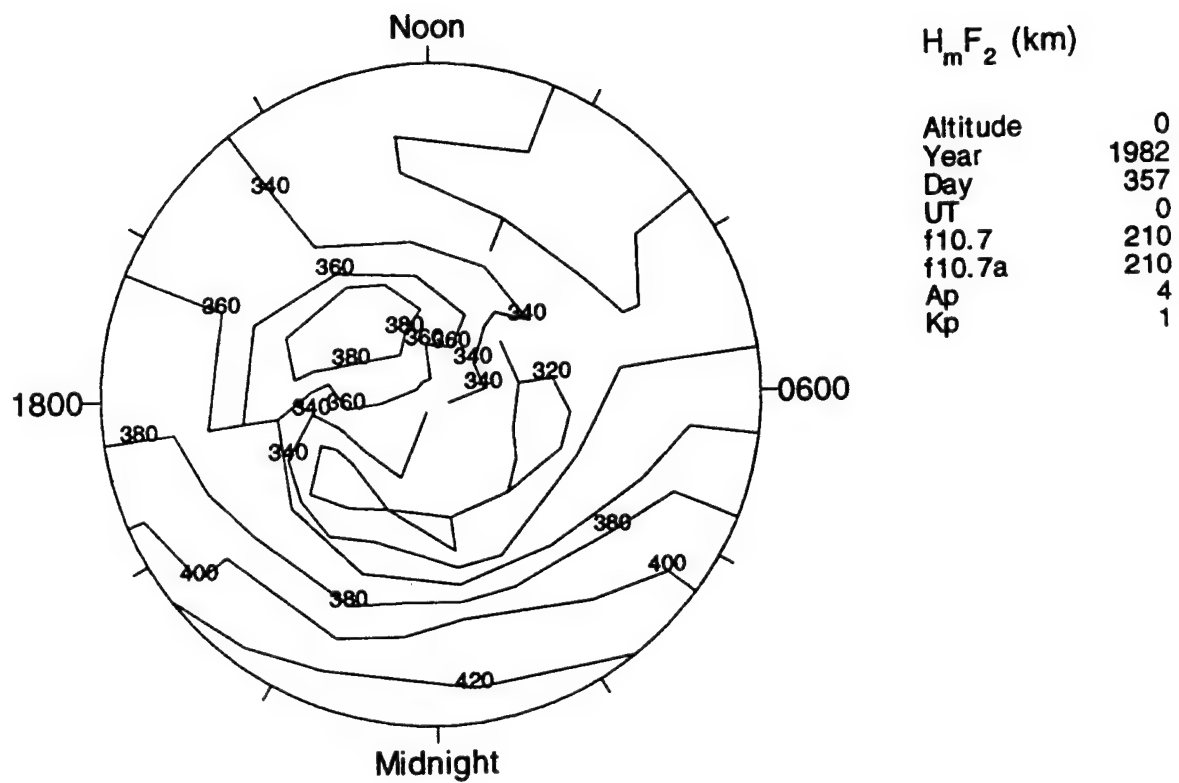


Figure 16c. Snapshot of the $h_m F_2$ at 0 UT. The conditions are the same as for Figure 16a.

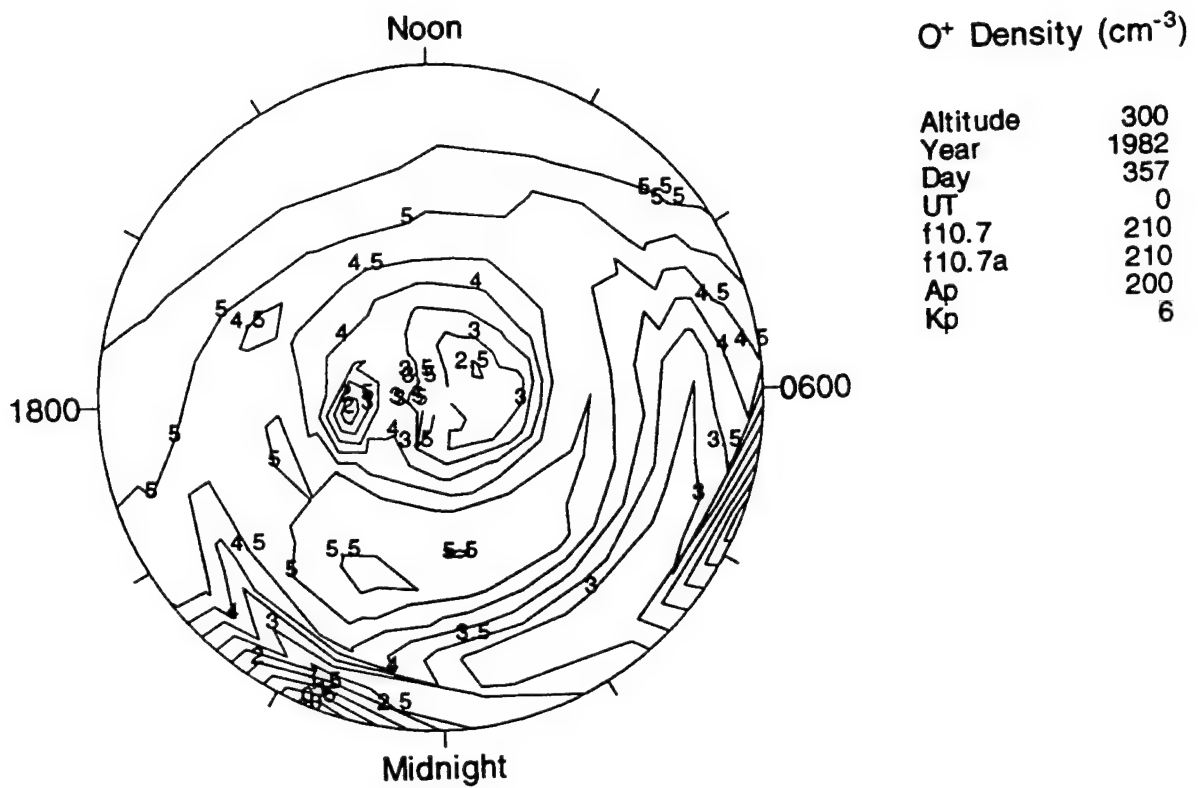


Figure 17a. Snapshot of the O⁺ density distribution at 300 km and 0 UT. The conditions represent solar maximum, winter, and high magnetic activity.

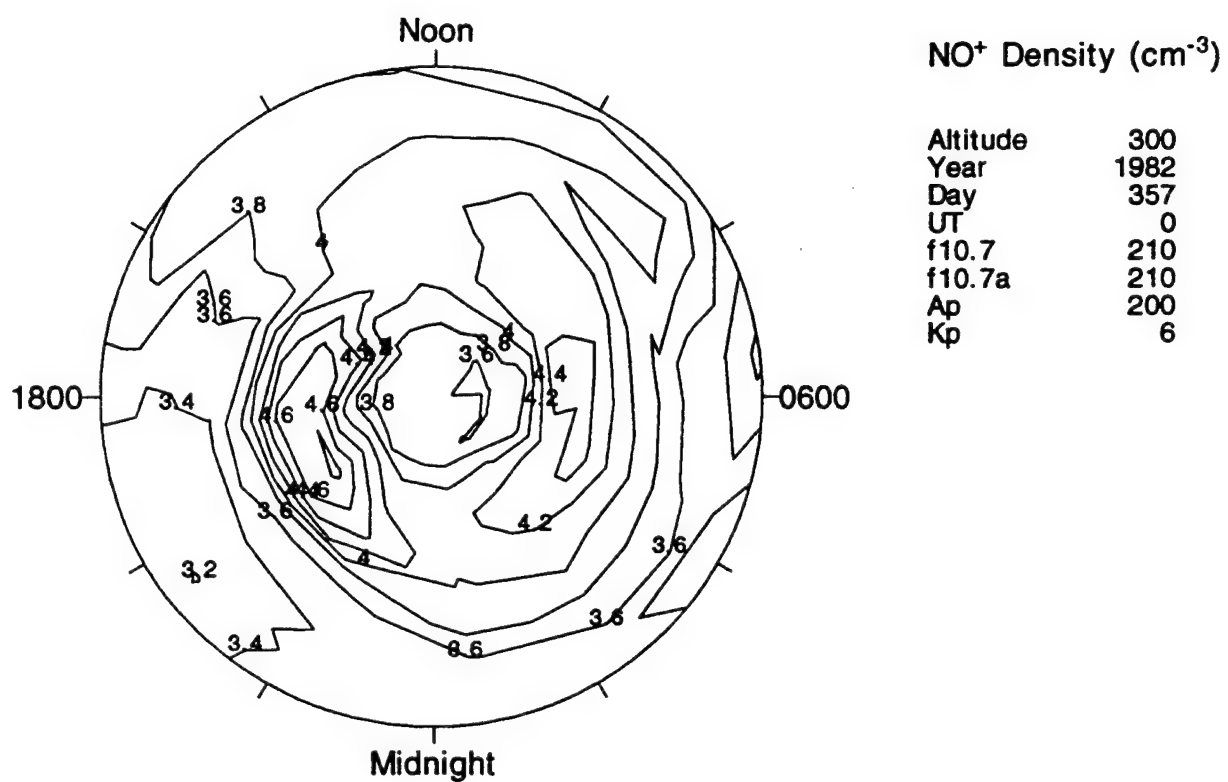


Figure 17b. Snapshot of the NO⁺ density distribution at 300 km and 0 UT. The conditions are the same as for Figure 17a.

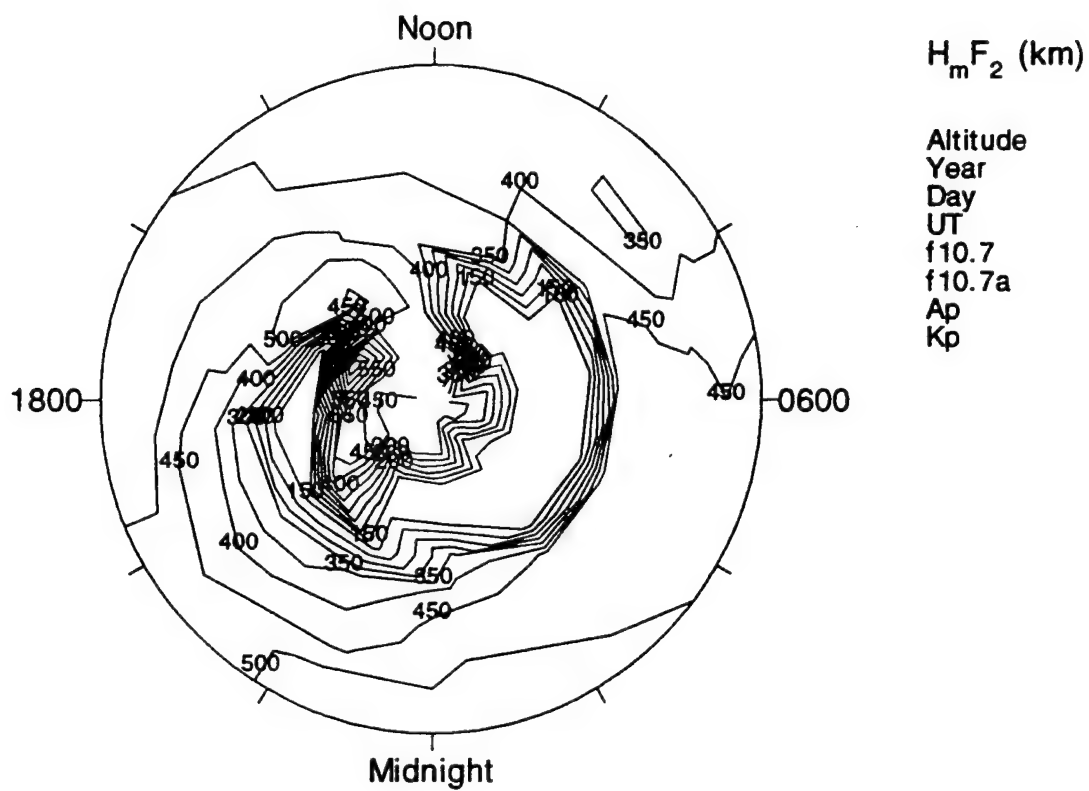


Figure 17c. Snapshot of the $h_m F_2$ at 0 UT. The conditions are the same as for Figure 17a.

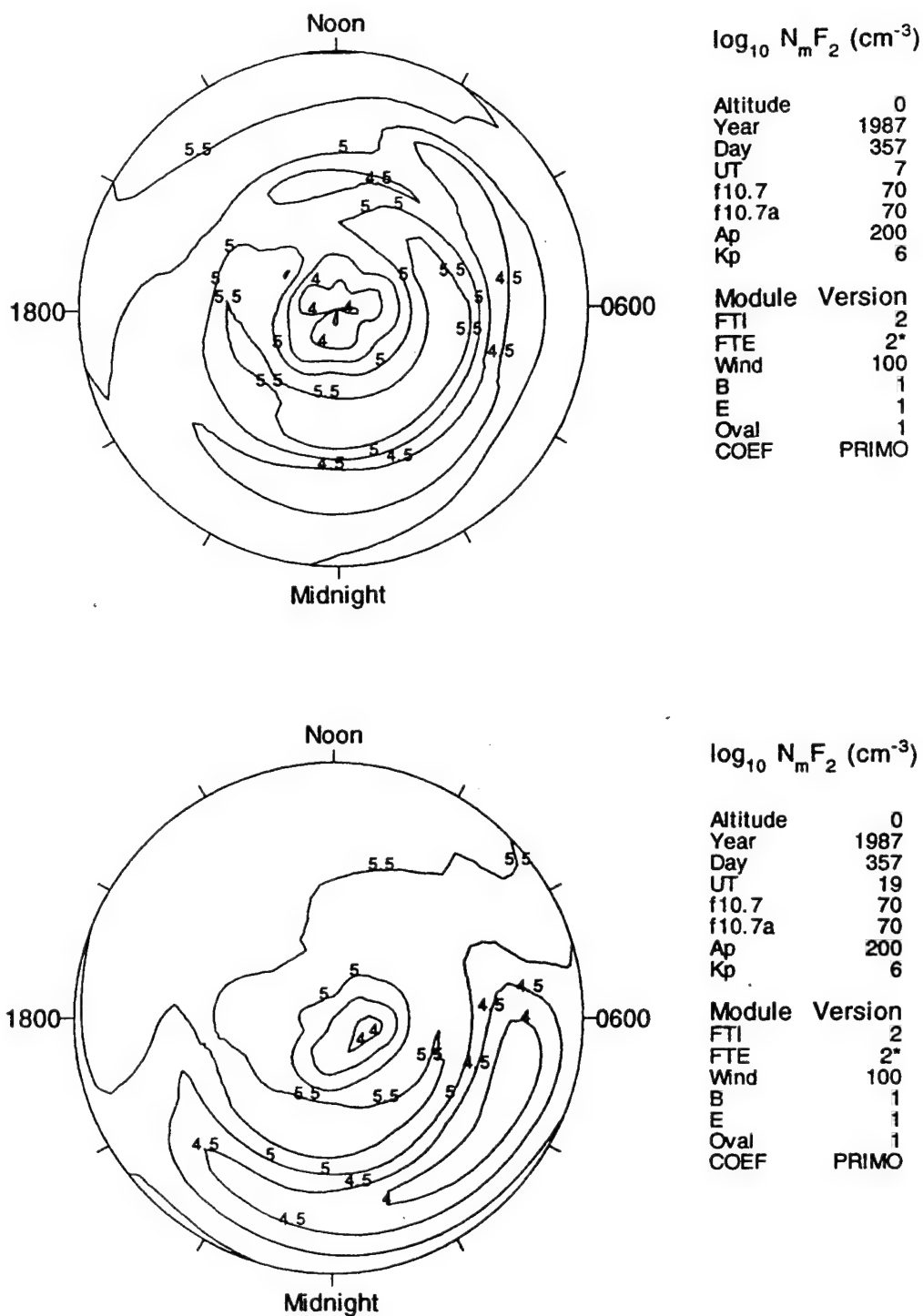
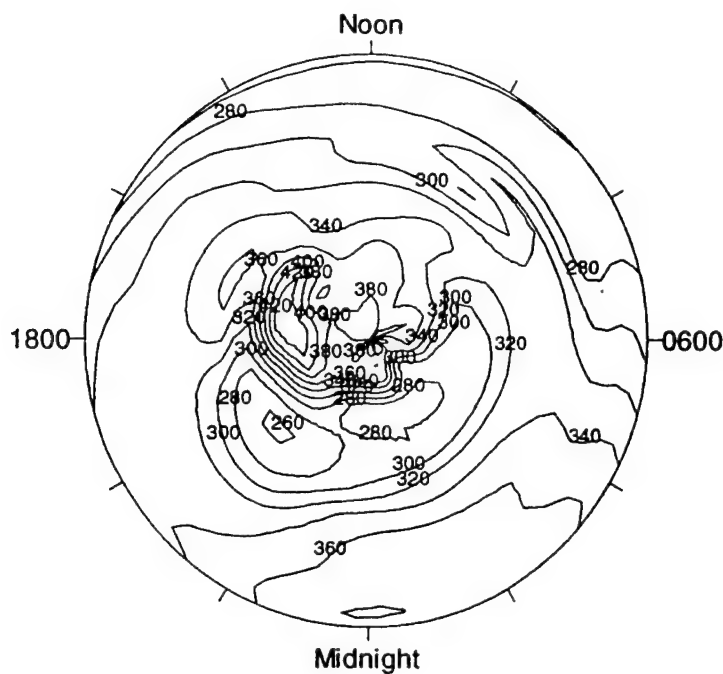


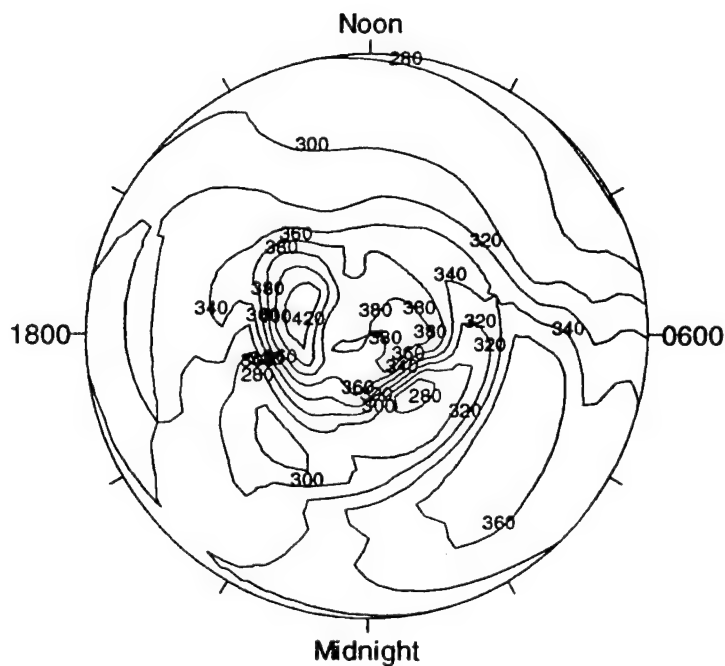
Figure 18a. Snapshots of the $N_m F_2$ distribution at 0700 UT (top panel) and 1900 UT (bottom panel). The conditions represent solar minimum, winter, and high magnetic activity.



$H_m F_2$ (km)

Altitude 0
 Year 1987
 Day 357
 UT 7
 f10.7 70
 f10.7a 70
 Ap 200
 Kp 6

Module Version
 FTI 2
 FTE 2*
 Wind 100
 B 1
 E 1
 Oval 1
 COEF PRIMO

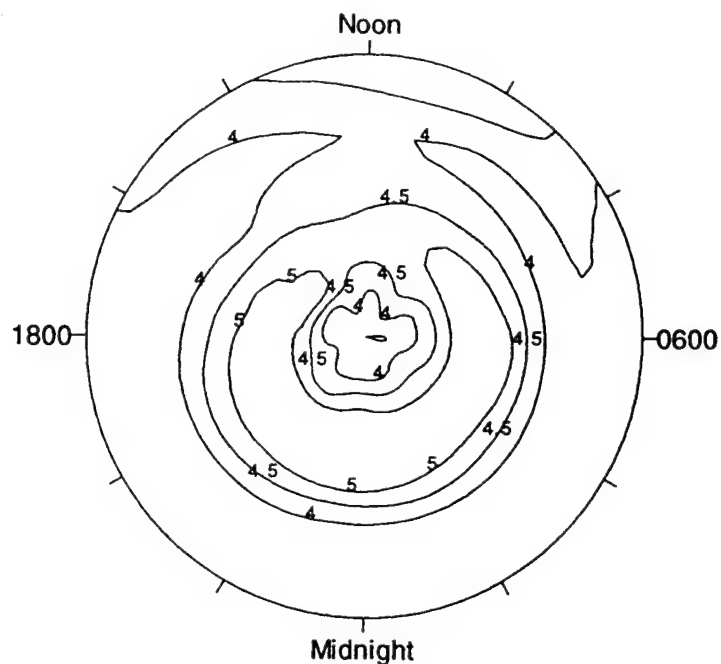


$H_m F_2$ (km)

Altitude 0
 Year 1987
 Day 357
 UT 19
 f10.7 70
 f10.7a 70
 Ap 200
 Kp 6

Module Version
 FTI 2
 FTE 2*
 Wind 100
 B 1
 E 1
 Oval 1
 COEF PRIMO

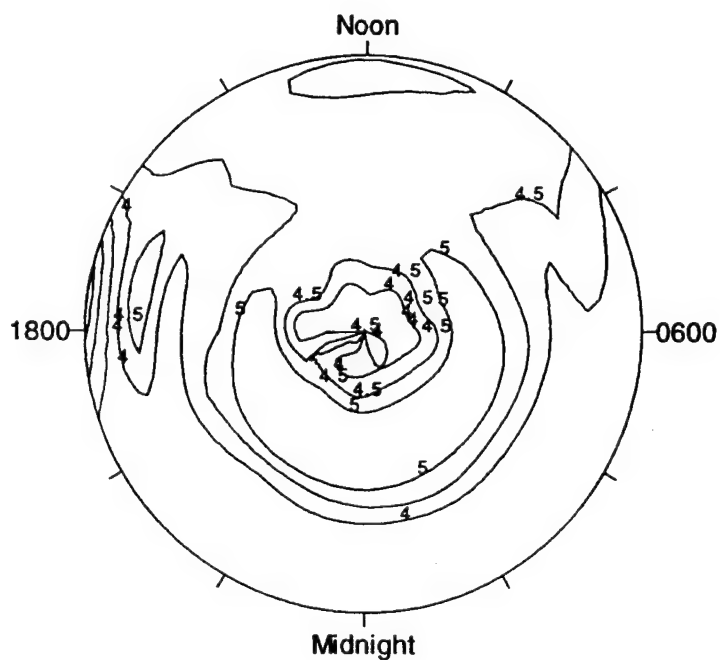
Figure 18b. Snapshots of the $h_m F_2$ distribution at 0700 UT (top panel) and 1900 UT (bottom panel). The conditions are the same as for Figure 18a.



$\log_{10} N_e \text{ (cm}^{-3}\text{)}$

Altitude 140
Year 1987
Day 357
UT 7
f10.7 70
f10.7a 70
Ap 200
Kp 6

Module Version
FTI 2
FTE 2*
Wind 100
B 1
E 1
Oval 1
COEF PRIMO



$\log_{10} N_e \text{ (cm}^{-3}\text{)}$

Altitude 140
Year 1987
Day 357
UT 19
f10.7 70
f10.7a 70
Ap 200
Kp 6

Module Version
FTI 2
FTE 2*
Wind 100
B 1
E 1
Oval 1
COEF PRIMO

Figure 18c. Snapshots of the electron density distribution at 140 km at 0700 UT (top panel) and 1900 UT (bottom panel). The conditions are the same as for Figure 18a.

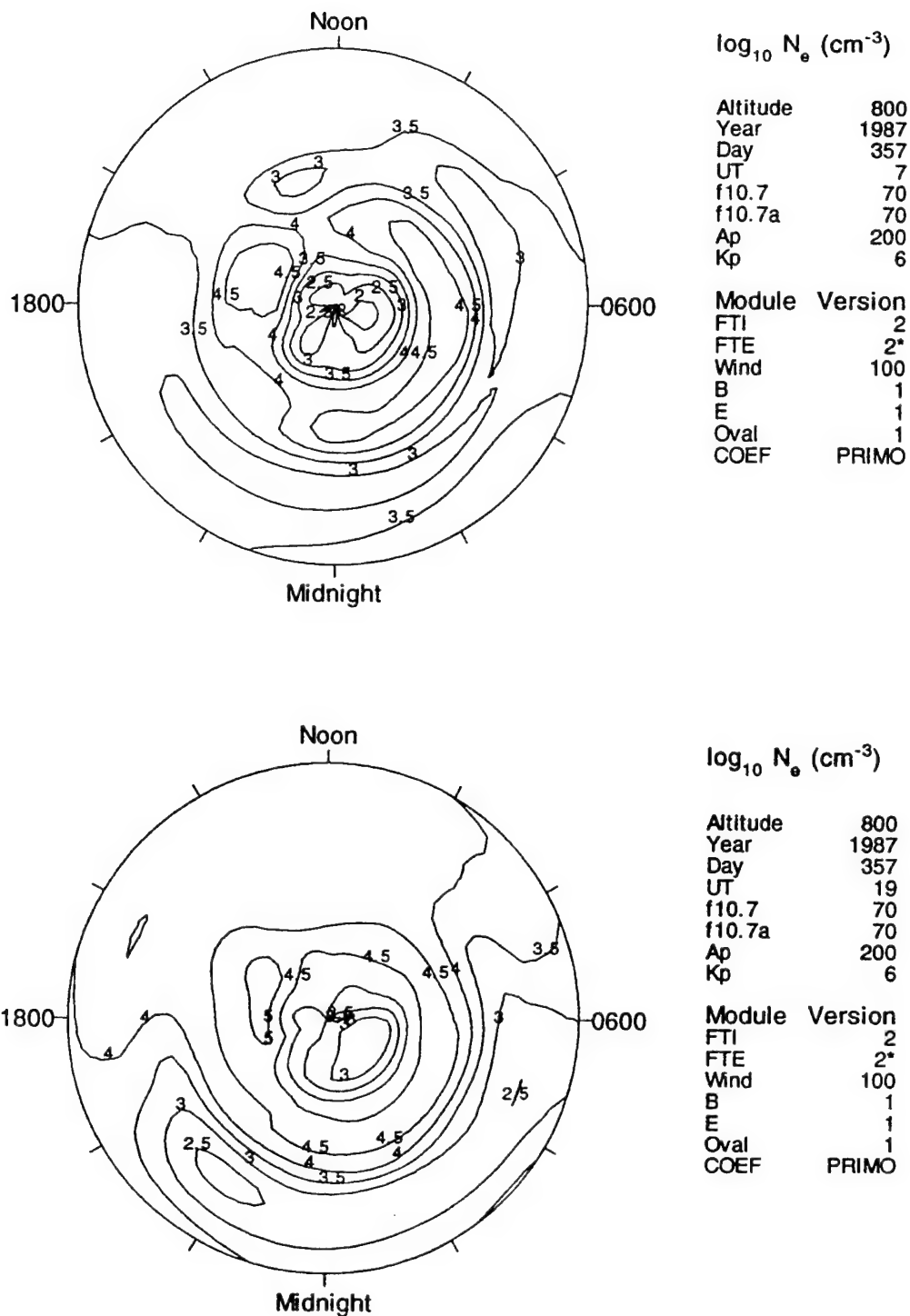
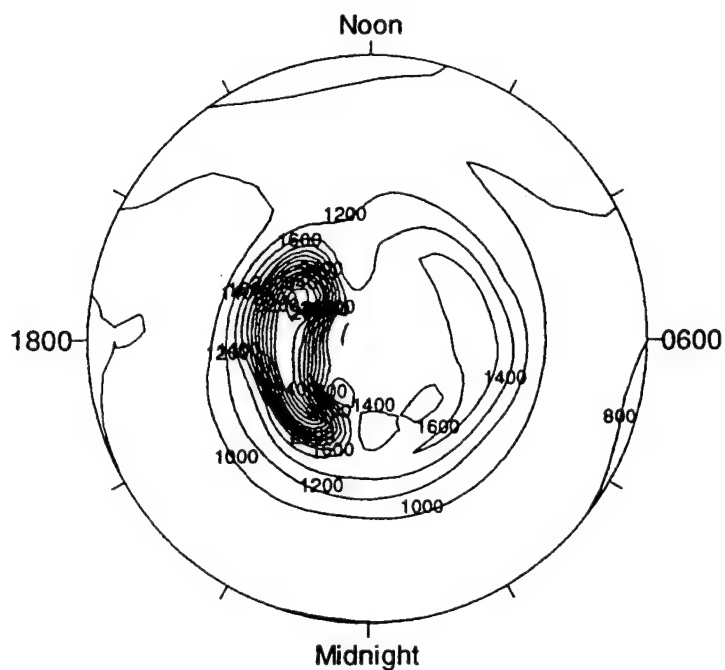


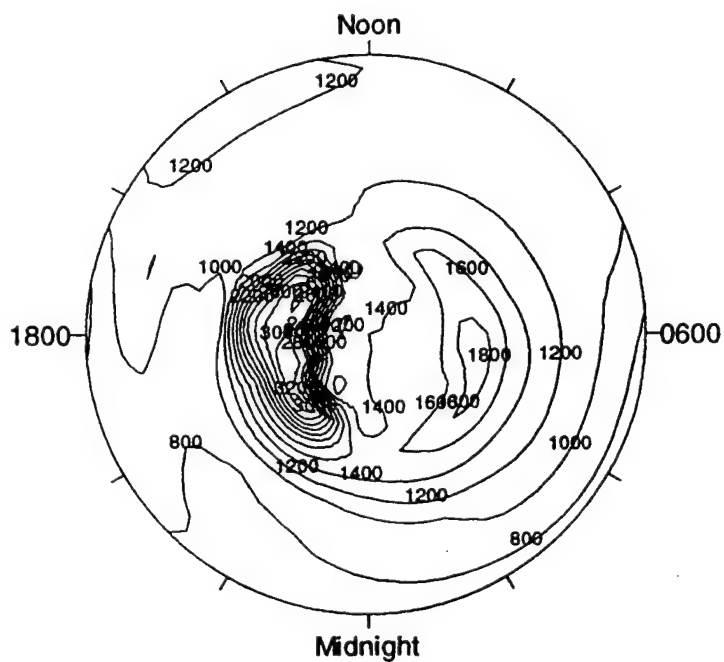
Figure 18d. Snapshots of the electron density distribution at 800 km at 0700 UT (top panel) and 1900 UT (bottom panel). The conditions are the same as for Figure 18a.



T_i (K)

Altitude 500
Year 1987
Day 357
UT 7
f10.7 70
f10.7a 70
Ap 200
Kp 6

Module Version
FTI 2
FTE 2*
Wind 100
B 1
E 1
Oval 1
COEF PRIMO

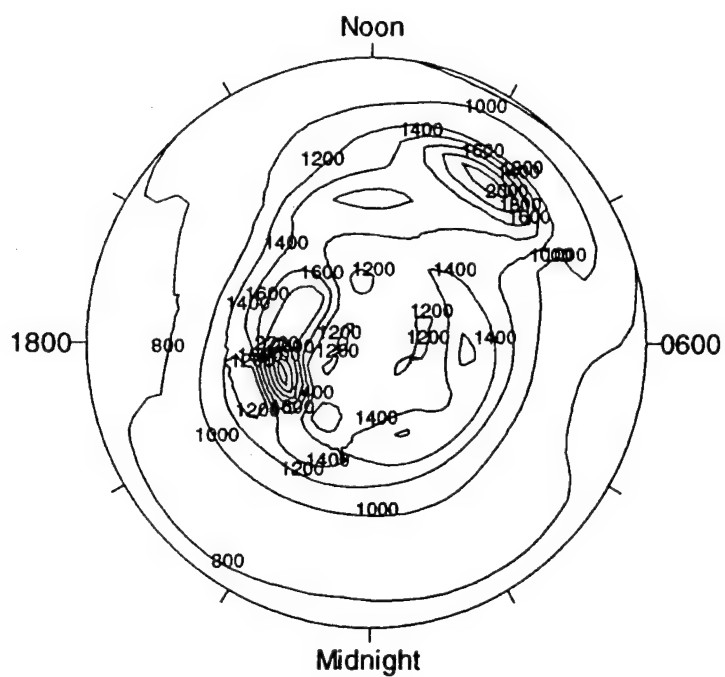


T_i (K)

Altitude 500
Year 1987
Day 357
UT 19
f10.7 70
f10.7a 70
Ap 200
Kp 6

Module Version
FTI 2
FTE 2*
Wind 100
B 1
E 1
Oval 1
COEF PRIMO

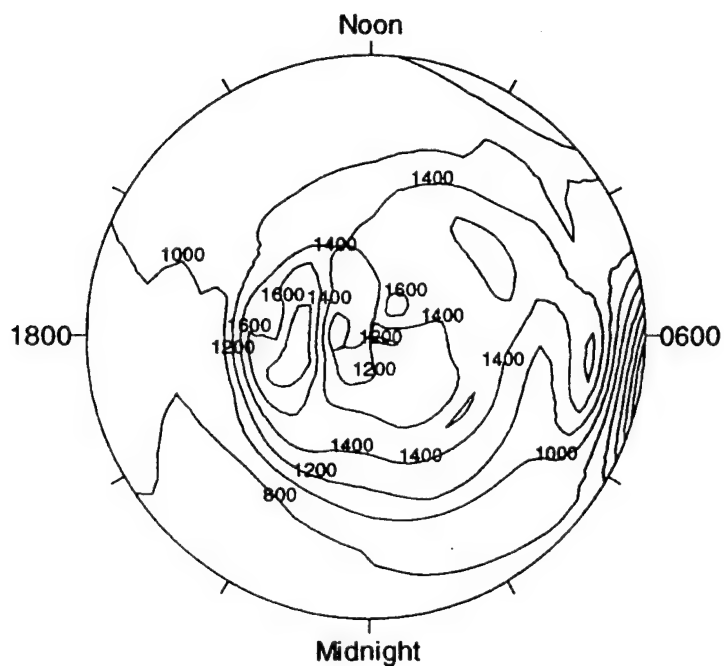
Figure 18e. Snapshots of the ion temperature distribution at 500 km at 0700 UT (top panel) and 1900 UT (bottom panel). The conditions are the same as for Figure 18a.



T_e (K)

Altitude 232
Year 1987
Day 357
UT 7
f10.7 70
f10.7a 70
Ap 200
Kp 6

Module Version
FTI 2
FTE 2*
Wind 100
B 1
E 1
Oval 1
COEF PRIMO



T_e (K)

Altitude 232
Year 1987
Day 357
UT 19
f10.7 70
f10.7a 70
Ap 200
Kp 6

Module Version
FTI 2
FTE 2*
Wind 100
B 1
E 1
Oval 1
COEF PRIMO

Figure 18f. Snapshots of the electron temperature distribution at 232 km at 0700 UT (top panel) and 1900 UT (bottom panel). The conditions are the same as for Figure 18a.

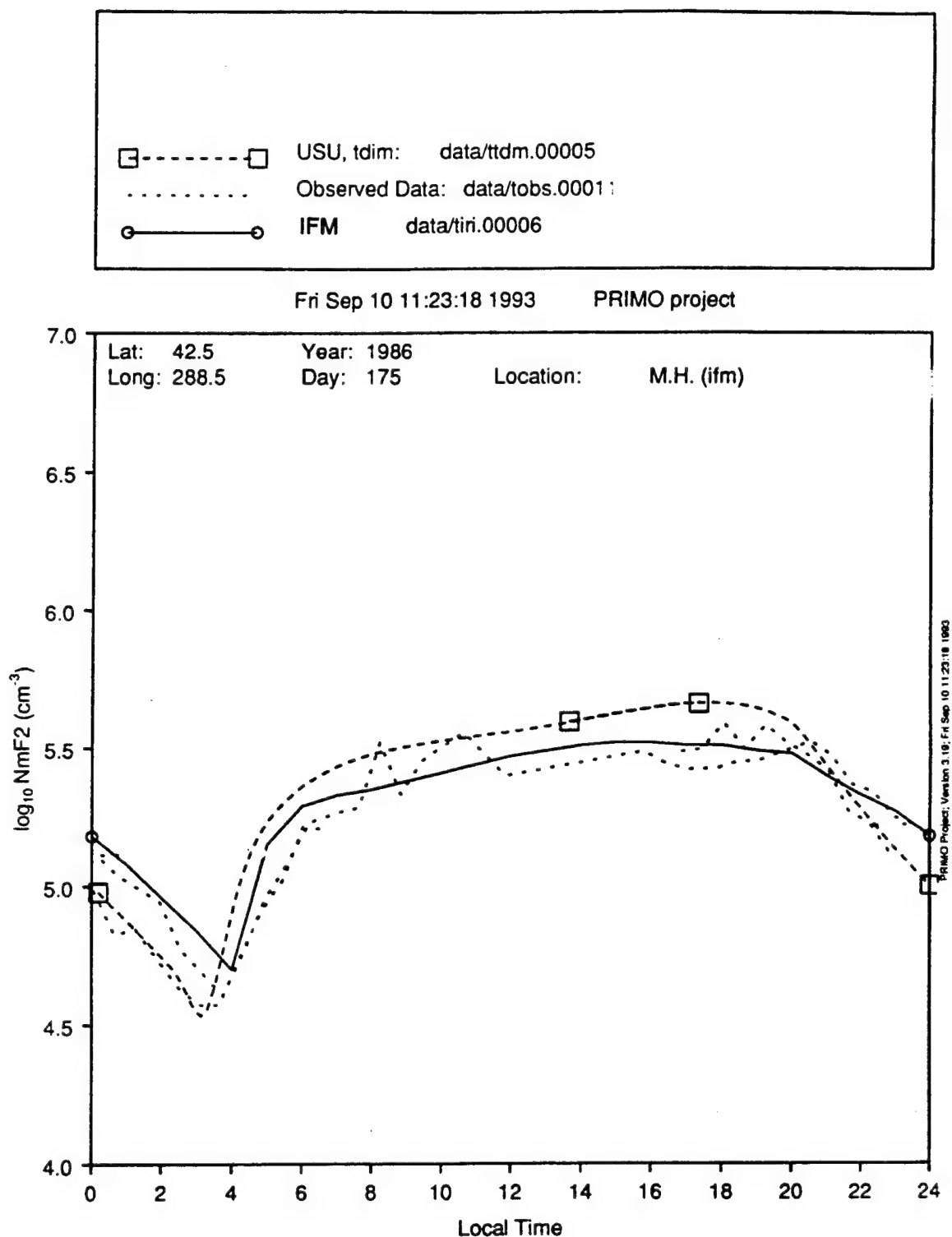


Figure 19a. Diurnal variations of N_mF_2 for Millstone Hill as obtained from the IFM (solid line), the TDIM (long dashed line) and incoherent scatter radar measurements (dotted line). The conditions are for solar minimum and summer.

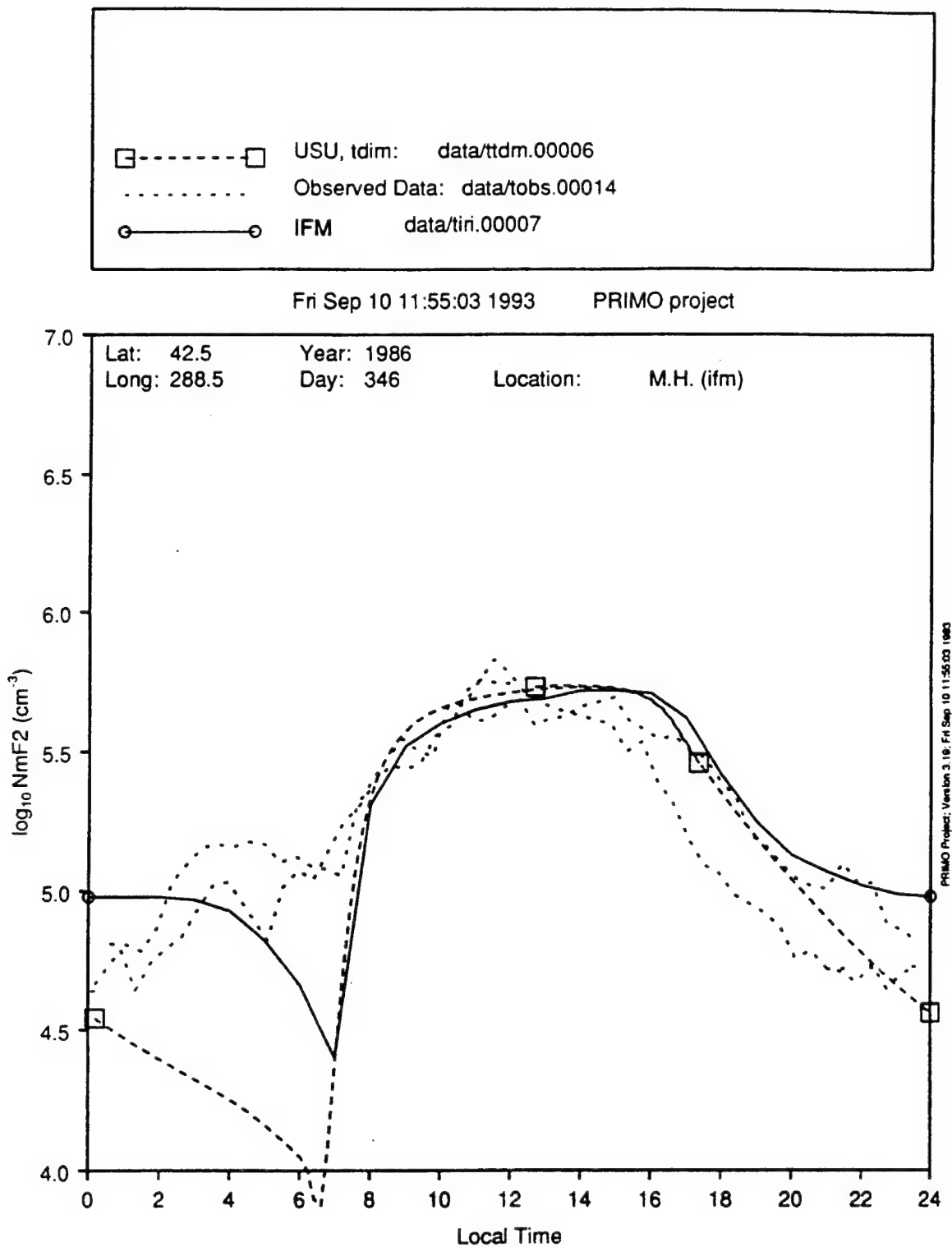


Figure 19b. Same as Figure 19a but for solar minimum and winter conditions.

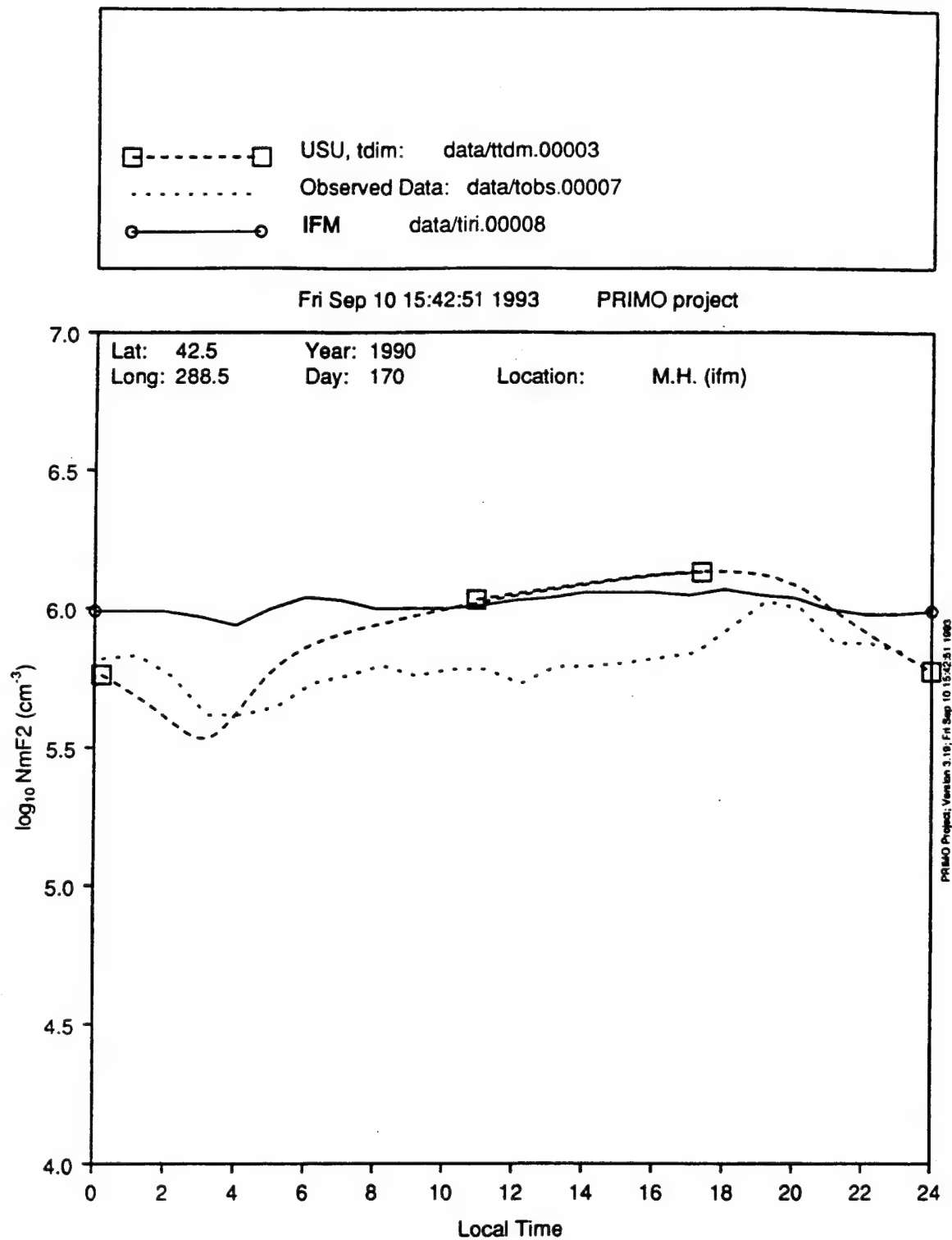


Figure 19c. Same as Figure 19a but for solar maximum and summer conditions.

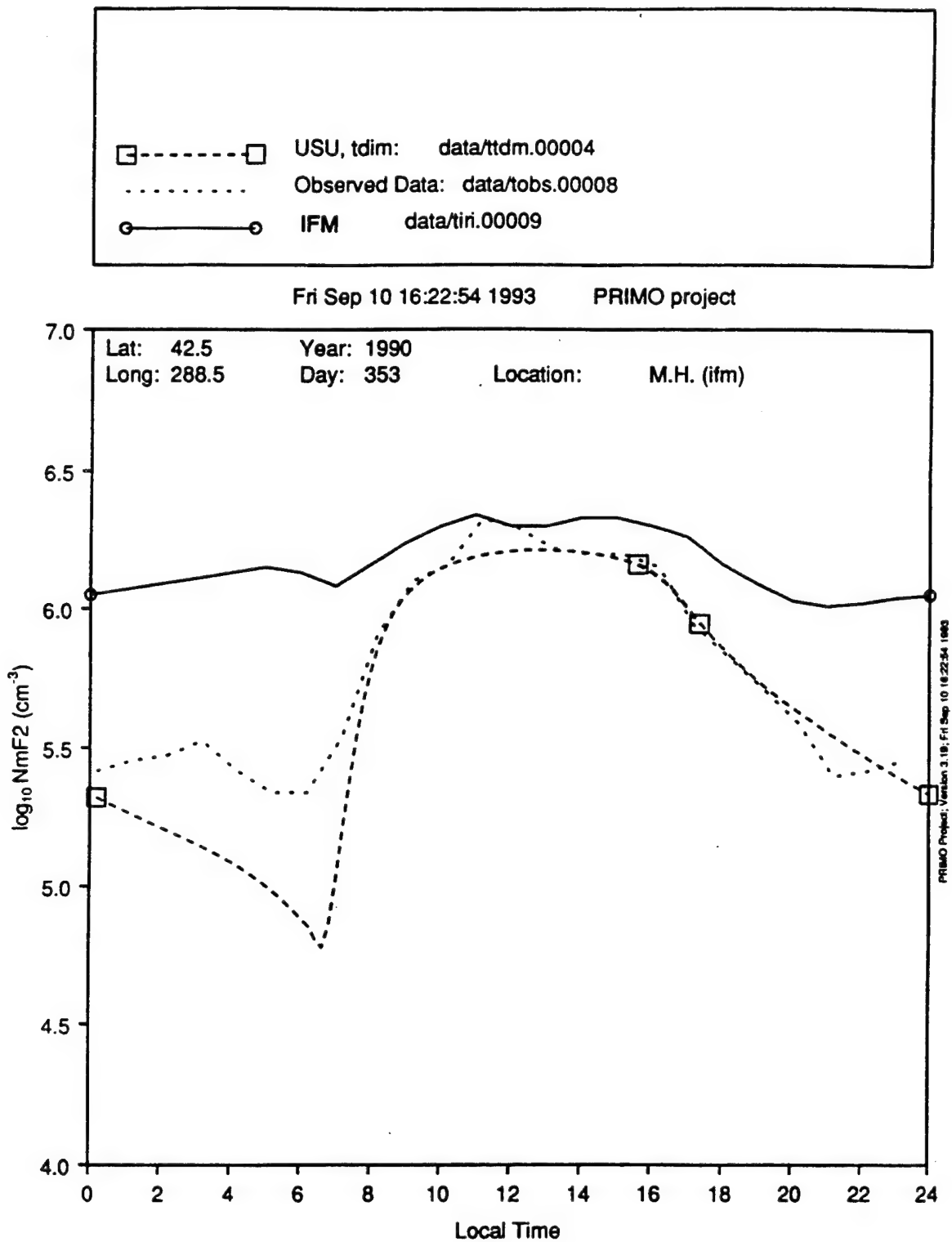


Figure 19d. Same as Figure 19a but for solar maximum and winter conditions.

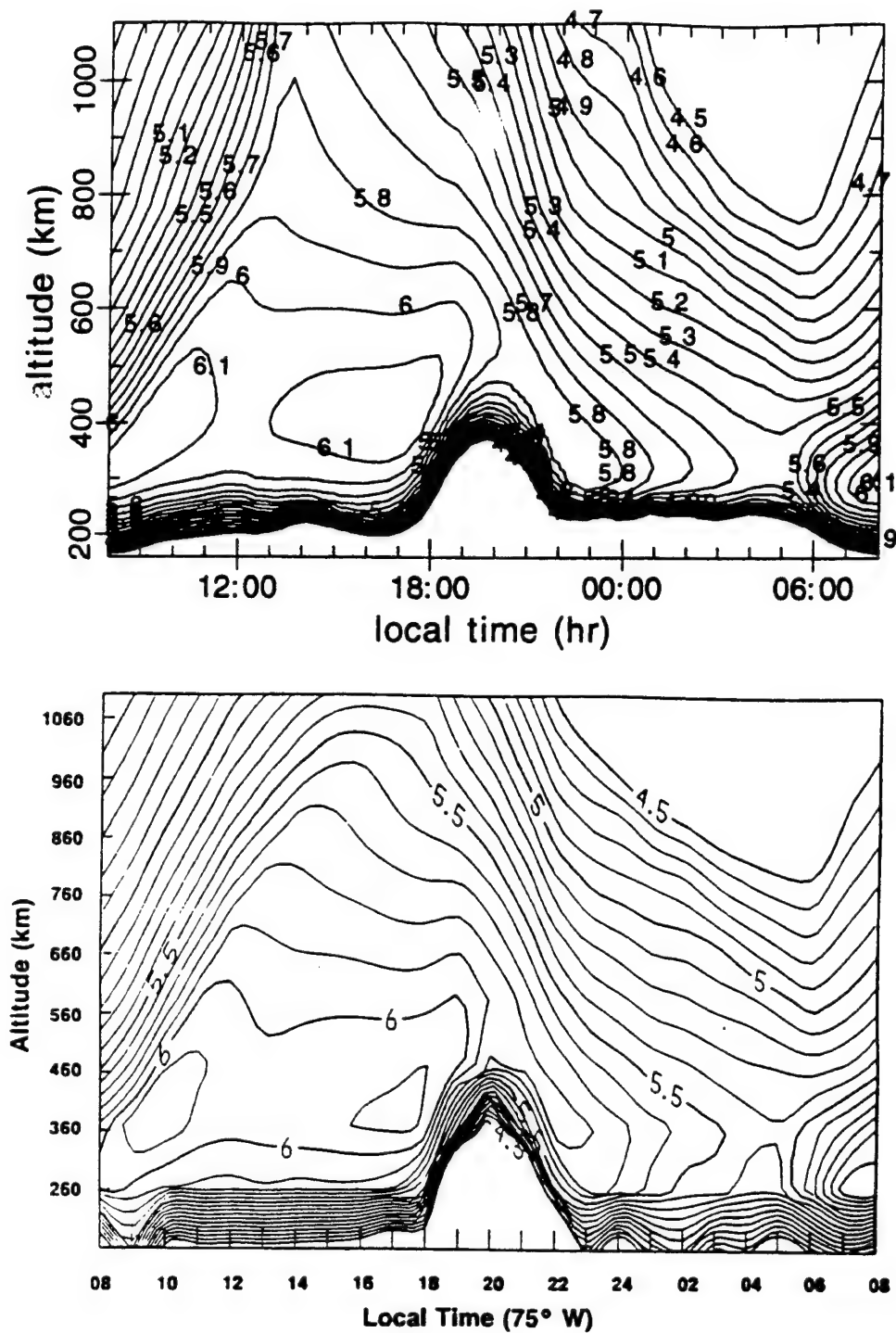


Figure 20. Comparison of the diurnal variation of the O^+ density over Jicamarca as calculated by the IFM (top panel) and by Preble et al (1994) using the Anderson equatorial model (bottom panel). The results are for medium solar conditions.

7. OPERATING MODE

The current version of the IFM is self-contained and can be run with the following few parameters:

Kp	(from 3 hours prior to the start time through the duration of the forecast)
F10.7	(solar flux)
Day	(decimal number)
Year	(gives solar cycle phase)
Start Time	(UT hours and minutes)
Forecast Duration	(hours and minutes)

The model can also be run with either a cold or a hot start. With a cold start, no initial global distribution of densities is required. However, if ionospheric densities from the PRISM model are available or if the output from a previous IFM run is available, the IFM can start from these densities and then forecast the subsequent change in the global density distribution. The initial global distribution of densities must be specified on the ICED grid.

The IFM was constructed in a modular form so that when real-time data are routinely available from the DMSP satellites and the DISS and TISS ground-based networks, they can be ingested to provide better plasma convection and particle precipitation patterns as well as better real-time density updates. The next phase of IFM development will probably contain this improvement, depending on data availability.

The global output database for each forecast time step is comprised of the following:

5 physical parameters: O^+ , molecular ion, H^+ , T_i , and T_e .

35 altitude steps: at different altitudes from 90 to 800 km.

60 latitude steps: at 2° intervals poleward of 50° and at 5° intervals equatorward of 50° .

24 longitude (MLT/LT) steps: at 15° intervals.

This corresponds to a total of 252,000 parameters per forecast. Assuming each is a 2 byte word, this is a 0.5 Mbyte dataset. If the IFM is running with a forecast every 15 minutes, then the IFM generates 2 Mbytes/hour. Any one of these datasets can be used to do a hot restart of the IFM. In 24 hours the database increases substantially, 48 Mbytes.

The database can be significantly compressed for other applications, examples of which are the following schemes:

(1) Peak electron density maps ($1 \times 1 \times 60 \times 24 \times 4 \times 2 = 11,520$ bytes/hr).

(2) N_e along satellite* orbit ($1 \times 1 \times 60 \times 2 \times 1.5 \times 2 = 360$ bytes/orbit).

(3) Northern high latitude TEC maps ($1 \times 1 \times 20 \times 24 \times 4 \times 2 = 3,840$ bytes/hr).

* assuming an ionospheric satellite orbit.

References

- Anderson, D.N., A theoretical study of the ionospheric F region equatorial anomaly, I. theory, Planet Space Sci., 21, 409-419, 1973.
- Anderson, D.N., Modeling the ambient, low latitude F region ionosphere - a review, J. Atmos. Terr. Phys., 43, 753-762, 1981.
- Chen, W.M., and R.D. Harris, An ionospheric E-region night-time model, J. Atmos. Terr. Phys., 33, 1193-1207, 1971.
- Feldstein, Y.I. and G.V. Starkov, Dynamics of auroral belt and polar geomagnetic disturbances, Planet Space Sci., 15, 209-229, 1967.
- Foster, J.C., An empirical electric field model derived from Chatanika radar data, J. Geophys. Res., 88, 981-987, 1983.
- Hardy, D.A., M.S. Gussenhoven and E. Holeman, A statistical model of auroral electron precipitation, J. Geophys. Res., 90, 4229-4248, 1985.
- Hedin, A.E., Extension of the MSIS thermosphere model into the middle and lower atmosphere, J. Geophys. Res., 96, 1159-1172, 1991.
- Hedin, A.E., et al, Revised global model of thermosphere winds using satellite and ground-based observations, J. Geophys. Res., 96, 7657-7688, 1991.
- Heelis, R.A., The effects of interplanetary magnetic field orientation on dayside high-latitude ionospheric convection, J. Geophys. Res., 89, 2873-2880, 1984.
- Heelis, R.A., J.K. Lowell and R.W. Spiro, A model of the high-latitude ionospheric convection pattern, J. Geophys. Res., 87, 6339-6345, 1982.
- Heppner, J.R. and N.C. Maynard, Empirical high-latitude electric field models, J. Geophys. Res., 92, 4467-4489, 1987.
- Knudsen, W.C., P.M. Banks, J.D. Winningham, and D.M. Klumpar, Numerical model of the convection F2 ionosphere at high latitudes J. Geophys. Res., 82, 4782-4792, 1977.
- Preble, A.J., D.N. Anderson, B.G. Fejer, and P.H. Doherty, Comparison between calculated and observed F region electron density profiles at Jicamarca, Peru, Radio Sci., 29, 857-866, 1994.
- Richmond, A.D., et al, An empirical model of quiet-day ionospheric electric fields at middle and low latitudes, J. Geophys. Res., 85, 4658-4664, 1980.
- Schunk, R.W., A mathematical model of the middle and high latitude ionosphere, PAGEOPH., 127, 255-303, 1988a.
- Schunk, R.W., Polar wind tutorial, In "Physics of Space Plasmas", SPI Conf. Proc. and Reprint Series, 8, 81-134, 1988b.
- Schunk, R.W., J.J. Sojka and M.D. Bowline, Theoretical study of the electron temperature in the high-latitude ionosphere for solar maximum and winter

- conditions, J. Geophys. Res., 91, 12041-12054, 1986.
- Sojka, J.J., Global scale, physical models of the F-region ionosphere, Rev. Geophys., 27, 371-403, 1989.
- Sojka J.J. and R.W. Schunk, A theoretical study of the global F region for June solstice, solar maximum, and low magnetic activity, J. Geophys. Res., 90, 5285-5298, 1985.
- Spiro, R.W., P.H. Reiff and L.H. Maher, Precipitating electron energy flux and auroral zone conductances: an empirical model, J. Geophys. Res., 87, 8215-8227, 1982.
- Sterling, D.L., W.B. Hanson, R.J. Moffett, and R.G. Baxter, Influence of electrodynamic drifts and neutral air winds on some features of the F2 region, Radio Sci., 4, 1005-1023, 1969.
- Strickland, D.J., D.L. Book, T.P. Coffey and J.A. Fedder, Transport equation techniques for the deposition of auroral electrons, J. Geophys. Res., 81, 2755, 1976.
- Torr, M.R. and D.G. Torr, Ionization frequencies for solar cycle 21: revised, J. Geophys. Res., 90, 6675, 1985.
- Volland, H., A model of the magnetospheric electric convection field, J. Geophys. Res., 83, 2695-2699, 1978.
- Wallis, P.D. and E.E. Budzinski, Empirical models of height integrated conductivities, J. Geophys. Res., 86, 125-137, 1981.

APPENDIX A.

When the coupled diffusion equations for O^+ and NO^+ are linearized in time, the equations take the following form:

$$\begin{aligned}\frac{\partial n_1}{\partial t} = & A_1 \frac{\partial^2 n_1}{\partial z^2} + A_2 \frac{\partial n_1}{\partial z} + A_3 n_1 \\ & + A_4 \frac{\partial^2 n_2}{\partial z^2} + A_5 \frac{\partial n_2}{\partial z} + A_6 n_2 + A_7\end{aligned}$$

$$\begin{aligned}\frac{\partial n_2}{\partial t} = & B_1 \frac{\partial^2 n_2}{\partial z^2} + B_2 \frac{\partial n_2}{\partial z} + B_3 n_2 \\ & + B_4 \frac{\partial^2 n_1}{\partial z^2} + B_5 \frac{\partial n_1}{\partial z} + B_6 n_1 + B_7\end{aligned}$$

$$D_2^1 = D_2 n_1$$

$$V_2 = D_2^1 Q_2$$

$$W_2 = \frac{Z_2 T_e}{T_2} D_2^1$$

$$B_1 = \left(\frac{1}{n_1} \right)^k D_2^1 + W_2 \left(\frac{n_2}{n_1 n_e} \right)^k$$

$$\begin{aligned} B_2 = & -U_1 + \frac{\partial D_2^1}{\partial z} \left(\frac{1}{n_1} \right)^k - D_2^1 \left(\frac{1}{n_1^2} \frac{\partial n_1}{\partial z} \right)^k \\ & + \frac{\partial W_2}{\partial z} \left(\frac{n_2}{n_1 n_e} \right)^k + V_2 \left(\frac{1}{n_1} \right)^k \\ & + W_2 \left(\frac{1}{n_1 n_e} \frac{\partial n_2}{\partial z} + \frac{1}{n_1 n_e} \frac{\partial n_e}{\partial z} \right)^k - W_2 \left(\frac{n_2}{n_1^2 n_e} \frac{\partial n_1}{\partial z} \right)^k \\ & - W_2 \left(\frac{2n_2}{n_1 n_e^2} \frac{\partial n_e}{\partial z} \right)^k \end{aligned}$$

$$\begin{aligned} B_3 = & -\frac{\partial U_1}{\partial z} + \frac{\partial W_2}{\partial z} \left(\frac{1}{n_1 n_e} \frac{\partial n_e}{\partial z} - \frac{n_2}{n_1 n_e^2} \frac{\partial n_e}{\partial z} \right)^k + \frac{\partial V_2}{\partial z} \left(\frac{1}{n_1} \right)^k \\ & - V_2 \left(\frac{1}{n_1^2} \frac{\partial n_1}{\partial z} \right)^k + W_2 \left(\frac{1}{n_1 n_e} \frac{\partial^2 n_e}{\partial z^2} - \frac{n_2}{n_1 n_e^2} \frac{\partial^2 n_e}{\partial z^2} \right)^k \\ & - W_2 \left(\frac{1}{n_1 n_e^2} \frac{\partial n_2}{\partial z} \frac{\partial n_e}{\partial z} \right)^k \\ & - W_2 \left(\frac{1}{n_1^2 n_e} \frac{\partial n_1}{\partial z} \frac{\partial n_e}{\partial z} - \frac{n_2}{n_1^2 n_e^2} \frac{\partial n_1}{\partial z} \frac{\partial n_e}{\partial z} \right)^k \end{aligned}$$

$$-W_2 \left[\frac{1}{n_1 n_e^2} \left(\frac{\partial n_e}{\partial z} \right)^2 - \frac{2n_2}{n_1 n_e^3} \left(\frac{\partial n_e}{\partial z} \right)^2 \right]^k - L_2$$

$$B_4 = W_2 \left(\frac{n_2}{n_1 n_e} \right)^k$$

$$\begin{aligned} B_5 = & \overbrace{D_2^1}^{(-)} \left(\frac{1}{n_1^2} \frac{\partial n_2}{\partial z} \right)^k + \frac{\partial W_2}{\partial z} \left(\frac{n_2}{n_1 n_e} \right)^k - V_2 \left(\frac{n_2}{n_1^2} \right)^k \\ & + W_2 \left(\frac{1}{n_1 n_e} \frac{\partial n_2}{\partial z} \right)^k - W_2 \left(\frac{n_2}{n_1^2 n_e} \frac{\partial n_1}{\partial z} + \frac{n_2}{n_1^2 n_e} \frac{\partial n_e}{\partial z} \right)^k \\ & - W_2 \left(\frac{2n_2}{n_1 n_e^2} \frac{\partial n_e}{\partial z} \right)^k \end{aligned}$$

$$\begin{aligned} B_6 = & \overbrace{\partial D_2^1}^{(-)} \left(\frac{1}{n_1^2} \frac{\partial n_2}{\partial z} \right)^k + D_2^1 \left(\frac{2}{n_1^3} \frac{\partial n_2}{\partial z} \frac{\partial n_1}{\partial z} \right)^k \\ & - D_2^1 \left(\frac{1}{n_1^2} \frac{\partial^2 n_2}{\partial z^2} \right)^k - \frac{\partial W_2}{\partial z} \left(\frac{n_2}{n_1 n_e^2} \frac{\partial n_e}{\partial z} + \frac{n_2}{n_e n_1^2} \frac{\partial n_e}{\partial z} \right)^k \\ & - \frac{\partial V_2}{\partial z} \left(\frac{n_2}{n_1^2} \right)^k - V_2 \left(\frac{1}{n_1^2} \frac{\partial n_2}{\partial z} \right)^k + V_2 \left(\frac{2n_2}{n_1^3} \frac{\partial n_1}{\partial z} \right)^k \\ & - W_2 \left(\frac{n_2}{n_1^2 n_e} \frac{\partial^2 n_e}{\partial z^2} + \frac{n_2}{n_1 n_e^2} \frac{\partial^2 n_e}{\partial z^2} \right)^k \\ & - W_2 \left(\frac{1}{n_e n_1^2} \frac{\partial n_2}{\partial z} \frac{\partial n_e}{\partial z} + \frac{1}{n_1 n_e^2} \frac{\partial n_2}{\partial z} \frac{\partial n_e}{\partial z} \right)^k \end{aligned}$$

$$\begin{aligned}
& + W_2 \left(\frac{n_2}{n_1^2 n_e^2} \frac{\partial n_1}{\partial z} \frac{\partial n_e}{\partial z} + \frac{2n_2}{n_e n_1^3} \frac{\partial n_1}{\partial z} \frac{\partial n_e}{\partial z} \right)^k \\
& + W_2 \left[\frac{n_2}{n_1^2 n_e^2} \left(\frac{\partial n_e}{\partial z} \right)^2 + \frac{2n_2}{n_1 n_e^3} \left(\frac{\partial n_e}{\partial z} \right)^2 \right]^k \\
B_7 = & P_2 + \frac{\partial D_2^1}{\partial z} \left(\frac{1}{n_1} \frac{\partial n_2}{\partial z} \right)^k - D_2^1 \left(\frac{1}{n_1^2} \frac{\partial n_2}{\partial z} \frac{\partial n_1}{\partial z} \right)^k \\
& + D_2^1 \left(\frac{1}{n_1} \frac{\partial^2 n_2}{\partial z^2} \right)^k + \frac{\partial W_2}{\partial z} \left(\frac{n_2}{n_1 n_e} \frac{\partial n_e}{\partial z} \right)^k + \frac{\partial V_2}{\partial z} \left(\frac{n_2}{n_1} \right)^k \\
& + V_2 \left(\frac{1}{n_1} \frac{\partial n_2}{\partial z} \right)^k - V_2 \left(\frac{n_2}{n_1^2} \frac{\partial n_1}{\partial z} \right)^k + W_2 \left(\frac{n_2}{n_1 n_e} \frac{\partial^2 n_e}{\partial z^2} \right)^k \\
& + W_2 \left(\frac{1}{n_1 n_e} \frac{\partial n_2}{\partial z} \frac{\partial n_e}{\partial z} \right)^k - W_2 \left(\frac{n_2}{n_e n_1^2} \frac{\partial n_1}{\partial z} \frac{\partial n_e}{\partial z} \right)^k \\
& - W_2 \left[\frac{n_2}{n_1 n_e^2} \left(\frac{\partial n_e}{\partial z} \right)^2 \right]^k
\end{aligned}$$

APPENDIX B
SUBROUTINE DESCRIPTIONS

Module: Coefficients
Calling Name: **ADCOEF**
Purpose: A routine that calculates the coefficients that appear in the coupled finite difference equations for O⁺ and NO⁺.

Module: Trajectory Follow - advance grid
Calling Name: **ANOTHERFLOW**
Purpose: Prior to following the trajectories for an IFM time interval the IFM grid is advanced in MLT by the time interval. This assures that corotational flux tubes stay at the midpoints of their cells and reduces the number of flux tubes needed.

Module: Atmospheric Densities and Temperatures.
Calling Name: **ATMOS**
Purpose: A routine that calculates the atmospheric densities and temperatures as a function of altitude at a specified location and time. A fast routine that is based on cubic spline fits to MSIS outputs. MSIS-90 model.

Module: Auroral Ionization
Calling Name: **AURORA**
Purpose: A routine that calculates the auroral ionization rates as a function of altitude at a specified location and time. A fast routine which has scaleable altitude profile shapes. The scaling factor being dependent on the auroral energy flux.

Module: Boundary Conditions
Calling Name: **BC**
Purpose: A routine that provides the lower boundary densities and the ion fluxes at the top boundary. Chemical equilibrium at bottom boundary and zero escape fluxes at top boundary.

Module: Coefficients
Calling Name: CBCOEF
Purpose: Coefficients associated with the double tridiagonal matrix inversion.

Module: Trajectory Follow - uniformity of flux tube distribution
Calling Name: CELLCHECK
Purpose: Every, typically 15 minutes of model time, this routine checks the distribution of flux tubes in the ionospheric grid. New flux tubes are created when grids are empty or old flux tubes dropped when too many flux tubes are in a single grid cell.

Module: Trajectory Follow - define cell coordinates.
Calling Name: CELLCOORDS
Purpose: Computes the latitude (DLAT) and Magnetic Local Time (MLT) of the center point of a specific grid cell on a variable grid or a variable grid.

Module: Chemical Reactions
Calling Name: CHEM
Purpose: A routine that calculates the ion and electron chemical reactions at a specified location and time. A fast routine which accounts for only the dominant chemical reactions.

Module: Diffusion Coefficients
Calling Name: DIFF
Purpose: A routine that calculates the ion diffusion coefficients as a function of altitude at a specified location and time. A fast routine that only includes the dominant collision processes and ignores ion temperature anisotropies.

Module: E-region ion and electron densities
Calling Name: EREGION
Purpose: A routine that calculates the ion and electron density profiles in the E-region at a specified location and time. The NO⁺, O₂⁺, N₂⁺ and O⁺ ions are allowed to have comparable densities. Chemical equilibrium is assumed.

Module: Trajectory Follow - create new trajcetories.
Calling Name: FILLCELLS
Purpose: During the trajectory following phase when an empty cell is detected, this routine creates a new trajectory at the center of that cell. It also follows that trajectory backwards to the previous time step to initialize its density, etc. The procedure is as follows: Finds empty cell, obtains new trajectory coordinates (CELLCOORDS), follows trajectory backwards one IFM time interval to obtain density profile (FLOWBACK), then reverses direction and covects to the present time (REVERSE), and adds it to the trajectory data base.

Module: Trajectory Follow - trajectory distribution printout
Calling Name: FILLHIST
Purpose: Creates record of the distribution of flux tubes after each IFM time period. A reduced diagnostic output compatible with an operational IFM. This diagnostic would only be called if needed.

Module: Trajectory Follow - follow all trajectories.
Calling Name: FLOW
Purpose: At each time step this routine must generate the trajectories for all plasma flux tubes. The program calls a heirarchy of routines including the modules representing the magnetospheric convection electric field (FLOWV3). Corotation is added in the FLOWV1 routine. Generic interface to a variety of convection electric field models. Also has the capability to handle a variable time increment when following a trajectory.

Module: Trajectory Follow - follow a trajectory backwards.
Calling Name: **FLOWBACK**
Purpose: Given the final location of a trajectory, it follows the trajectory backwards in time to obtain its initial location at the prior IFM time interval.

Module: Trajectory Follow - convection model
Calling Name: **FLOWV3**
Purpose: Routine to specify the magnetospheric electric potential in the ionosphere. The Heppner and Maynard [1987] convection model is called by FLOWV3. For this initial level the input is k_p with the assumption that the A pattern is appropriate. At this level no dependence upon the interplanetary magnetic field is used. The variation of the cross polar potential with k_p follows closely the formula: cross tail potential = $(20 + 14 * k_p)$ KV.

Module: F-region ion and electron densities
Calling Name: **FREGION1**
Purpose: A routine that calculates the ion and electron density profiles in the F-region at a specified location and time. O^+ is assumed to be the only major ion. The NO^+ formulation includes diffusion, but it is assumed to be a major ion. O_2^+ and N_2^+ are assumed to be major ions in chemical equilibrium.

Module: F-region ion and electron densities
Calling Name: **FREGION2**
Purpose: A routine that calculates the ion and electron density profiles in the F-region at a specified location and time. Both O^+ and NO^+ are assumed to be major ions and both are based on a diffusion formulation. O_2^+ and N_2^+ are assumed to be minor ions in chemical equilibrium.

<u>Module:</u>	Density and Temperature Gradients
<u>Calling Name:</u>	GRADS
<u>Purpose:</u>	A routine that calculates electron and ion density gradients for a multi-step spatial grid.

<u>Module:</u>	Trajectory Follow - initialize the convection electric field.
<u>Calling Name:</u>	INITACTV
<u>Purpose:</u>	Initialize the convection electric field routines. Define the kp and other proxy indices. IFM uses this routine to interact with the AWS geophysical indices. A time series of the indices is read in and the program interpolates as needed to drive IFM with a time varying skp and other indices.

<u>Module:</u>	Trajectory Follow - grid initialization
<u>Calling Name:</u>	INITGRID
<u>Purpose:</u>	Initialize the IFM grid. Generic global routine which is driven by a latitude and longitude grid specification.

<u>Module:</u>	Trajectory Follow - initialize trajectories.
<u>Calling Name:</u>	INITTRAJ
<u>Purpose:</u>	At the start of an IFM run a grid is specified by INITGRID and geophysical conditions by INITACTV. These data are then used by this routine to initialize trajectories to be followed. Places flux tubes at the center of grid cells. Can be run with an uneven grid system.

<u>Module:</u>	Altitude Parameters
<u>Calling Name:</u>	ONE
<u>Purpose:</u>	A routine that calls the other subroutines which provide parameters as a function of altitude (CHEM, DIFF, etc.) at a specified location and time. The routine also calculates derivatives and coefficients for the PDE's. A new routine that allows for different spatial step sizes in the E and F regions.

Module: Auroral Precipitation
Calling Name: OVAL
Purpose: To define at a given location and time the auroral energy flux and the auroral characteristic energy. Improved Hardy auroral oval model.

Module: Photoionization
Calling Name: PHOTO
Purpose: A routine that calculates the solar EUV ionization rates as a function of altitude at a specified location and time. Ionization rates are calculated only for zenith angles less than 90°, and ionization frequencies are used for altitudes above 300 km.

Module: Coefficients
Calling Name: RECOEF
Purpose: A routine that calculates the coefficients for a double tridiagonal matrix inversion.

Module: Night Sector Ionization
Calling Name: RESONANT
Purpose: A routine that calculates the night-time ionization rates as a function of altitude at a specific location and time. A fixed set of ionization profiles, mainly associated with resonantly scattered Lyman Alpha.

Module: Trajectory Follow - reverses a backwards trajectory
Calling Name: REVERSE
Purpose: Reverses the order of the trajectory steps from FLOWBACK and adds this trajectory to the trajectory database.

Module: Solar Spectrum

Calling Name: SOLAR

Purpose: Defines the solar spectrum on a given day. A 39 wavelength spectrum that has been adapted to 11 bins and used in the TDIM. Very fast, depends upon F10.7.

Module: Matrix Inversion

Calling Name: SOLVER

Purpose: A routine that inverts a tridiagonal matrix for one partial differential equation.

Module: Electron Temperature

Calling Name: TE

Purpose: A routine that calculates the electron temperature as a function of altitude at a specified location and time. A fast routine that contains thermal conduction, but includes only the dominant heating and cooling processes.

Module: Ion Temperature

Calling Name: TI

Purpose: A routine that calculates the ion temperature as a function of altitude at a specified location and time. A fast routine that calculates the ion temperature assuming local heating and cooling processes dominate.

Module: Top Boundary Conditions

Calling Name: TOPDEN

Purpose: A routine that calculates the top boundary conditions for O^+ and NO^+ . The ionosphere is allowed to breathe, but no ions are allowed to escape to the magnetosphere.

Module: Neutral Wind

Calling Name: WIND

Purpose: A routine which provides horizontal wind speeds at a specified location and time. Altitude variations are included. MSIS wind model.

APPENDIX C.

Below is a summary of the papers in which the physics and chemistry contained in the ionospheric model have been validated. Highlights of the studies are listed in bullit form.

HIGH LATITUDES

1. Sojka et al. (*JGR*, 86, 2206, 1981)
 - AE-C satellite data at 300 km
 - High latitude regions where a given molecular ion dominates
 - Model predicted correct molecular ion
2. Sojka et al. (*JGR*, 87, 1711, 1982)
 - DMSP F2 and F4 satellites at 800 km
 - Quiet magnetic conditions
 - Diurnal dependence of Ne at high latitudes
 - Model predicted correct modulation and phase
3. Sojka et al. (*JGR*, 88, 7783, 1983)
 - Millstone Hill Radar
 - Convection pattern obtained from radar over 24-hour period
 - Corresponds to 'average' convection pattern
 - Model Ne at 500 km in general agreement with measurement
4. Murrin et al. (*PSS*, 32, 47, 1984)
 - Chatanika Radar
 - Quiet and disturbed days
 - Inferred vertical $E \times B$ & wind components
 - Comparison of diurnal variation of Ne
 - Good agreement with data for quiet day
 - Qualitative agreement with data for disturbed day
5. Sojka et al. (*PSS*, 33, 1375, 1985)
 - DMSP F4 satellite at 800 km

- Dayside mid-latitude trough in southern & northern hemispheres
 - Longitudinal dependence, depth, and asymmetry between North and South troughs were in agreement with measurements
6. Rasmussen et al. (*JGR*, 91, 6986, 1986)
- Simultaneous Chatanika & Millstone Hill data
 - Coherent scatter radar
 - NOAA-6 satellite
 - Convection pattern from radar data
 - Auroral precipitation pattern from satellite data
 - Generally good agreement between modelled and observed N_e (25%)
7. Rasmussen et al. (*JGR*, 93, 1922, 1988)
- Continuation of study 6 for T_e & T_i
 - Very good agreement between measured & modelled temperatures
 - Topside heat flux is important
8. Berkey et al. (*Polar Res.*, 48, 278, 1987)
- Halley Bay & Siple HF Sounders
 - Summer & Winter Conditions
 - N_mF_2 & h_mF_2 comparisons
 - Generally good agreement between modelled and measured values
 - Summer h_mF_2 's sensitive to wind
9. Sica et al. (*JATP*, 50, 141, 1988)
- EISCAT radar
 - Large downward ion drifts [>400 m/s] parallel to \mathbf{B} that persist for hours deduced from data
 - Model shows measurements were probably not interpreted correctly
10. Rasmussen et al. (*JGR*, 93, 9831, 1988)
- Arecibo and Chatanika Radars

- Compared modelled and measured densities in 85-220 km range
 - Solar maximum & minimum
 - Generally good agreement for a wide range of conditions
11. Sojka et al. (*JGR*, 95, 15275, 1990)
- IGY Ionosondes
 - Mid-latitude trough exhibits strong magnetic activity and longitude variations (Whalen, 1987)
 - Very good agreement between modelled and measured variations
12. Sojka et al. (*Adv. Space Res.*, 11, 39, 1991)
- Numerous satellites
 - Hoegy & Grebowsky (1989) mapped morphology of ionospheric polar hole for different solar cycle, seasonal UT, and K_p conditions
 - Model correctly predicted the observed features
13. Sojka et al. (*JGR*, 97, 1245, 1992)
- DE-2 Satellite
 - E-field & particle data along orbit
 - Auroral image sequence
 - Convection & precipitation inputs to model constrained
 - Modelled & measured Ne compared
 - Generally good agreement for quiet day
 - Discrepancies during substorm related to lack of adequate convection input

MID-LATITUDES

14. Sojka et al. (*JATP*, 50, 1027, 1988)
- Argentine Islands Ionosonde
 - Quiet magnetic activity
 - Monthly diurnal f_oF₂ curves from solar minimum to maximum

- Excellent agreement between modelled & measured f_oF_2
 - Neutral wind is critical for modelling
15. Wilkinson et al. (*Annl. Geophys.*, 6, 31, 1988)
- 10 Low and Mid-Latitude Ionosondes
 - N_mF_2 diurnal variation
 - Mid-latitude comparisons depend critically on wind
 - Low-latitude comparisons depend critically on ExB drifts
16. Sica et al. (*JGR*, 95, 8271, 1990)
- 41 Ionosondes
 - Mid-latitudes
 - Simultaneous data
 - Northern and Southern hemispheres
 - Diurnal variation of N_mF_2 compared
 - Winds are critical for modelling
17. Szuszczewicz et al. (*Adv. Space Res.* in press, 1993)
- 12 Soviet Ionosondes
 - 30-day-averaged diurnal N_mF_2
 - Excellent agreement with IRI
 - Winds are critical for modelling